

High order ghost-FEM for incompressible Navier-Stokes equations on moving domains

Hridya Dilip, Clarissa Astuto, Armando Coco and Giovanni Russo

July 2025

Abstract

We develop a new numerical technique for approximating solutions of the Navier–Stokes equations on moving domains. The method aims at simulating an incompressible fluid past an object whose motion is assigned *a priori* using a level-set function. The proposed approach relies on a space discretization based on the ghost finite element method (ghost-FEM), which allows computations on unfitted meshes and avoids costly remeshing as the domain evolves in time. Time integration is performed using an IMplicit-EXplicit (IMEX) scheme to address the nonlinearity of the convective term, ensuring high-order accuracy for incompressible flows. The error introduced by the geometrical approximation is handled using the Shifted Boundary Method, which allows higher order approximations of boundary conditions on unfitted meshes. Dirichlet boundary conditions are imposed weakly by means of Nitsche’s method. The associated stabilization parameter is chosen by solving a generalized eigenvalue problem, ensuring stability and accuracy of the numerical scheme. We present a series of numerical experiments designed to validate the accuracy of the proposed method, as well as comparisons with established benchmark problems involving moving boundaries.

1 Introduction

A wide variety of fluid dynamics phenomena can be modeled using the unsteady incompressible Navier–Stokes equations. These equations capture the behavior of flows in environments such as the atmosphere, oceans, rivers, and lakes, as well as in industrial systems such as turbines, aircraft engines, and vehicles [62]. Another well-studied problem is the flow of surfactants around a moving trap [55, 56, 36, 41, 47], that motivated the development of the method proposed in this paper. Aqueous surfactants play a key role in various biological, biochemical, and industrial processes. They influence foam stability [21], wettability, and coating flows [57], and are commonly applied as sprays to enhance the effectiveness of foliar-applied agrochemicals by improving pesticide penetration into plant foliage [39]. The influence of surfactants on the deformation of drops and bubbles [46, 47], and on the surrounding flow field, remains an area of active research, not only for its relevance to polymer and emulsion technologies, but also for the insights it offers into the complex physics of viscous interfacial flows [59]. Surfactant molecules act as a buffer between the fluid phases across an interface, modifying intermolecular forces and reducing surface tension in proportion to the local surfactant concentration [1]. For this reason, computing two-phase flows with surfactant has been challenging due to the associated interface dynamics, surface convection–diffusion of surfactants, fluid dynamics of the underlying Stokes or Navier–Stokes flows, and the coupling among them via the surface tension [63, 64, 36, 5].

From a numerical perspective, the Navier–Stokes equations have been extensively studied [40], using finite differences [58, 24, 5, 9], finite element [37, 32] and finite volume [42, 43] methods, and in [33] a finite element scheme based on coupled arbitrary Lagrangian–Eulerian (for the velocity) and Lagrangian approach (for the concentration of surfactants) is developed for the computation of interface flows with soluble surfactants. Many numerical schemes use a level-set

function to compute two-phase flows with surfactants [64, 36], and they are dissolved in the bulk fluid but also exist in adsorbed form on the interface separating two immiscible fluids.

Among the time discretizations, we have θ -method, such as Crank-Nicolson, or the projection method, proposed by Chorin in [23, 20]. It consists of a fractional step, where the velocity field is advanced in time by discretizing the momentum equation and ignoring the pressure term, obtaining a fictitious velocity that is not divergence-free. This velocity is then corrected by the pressure term by enforcing the divergence-free condition. Other approaches in time are the IMEX schemes [16], semi-implicit strategies designed to deal with nonlinear terms and high stiffness. They have been employed in a wide variety of applications, including the design of Asymptotic Preserving methods for the inviscid [17] and viscous [18, 28] compressible flows. IMEX schemes offer a suitable and flexible approach when aiming for higher-order time integration [7], and here we illustrate their performance in the context of Navier-Stokes equations and moving domains.

For the spatial discretization we use the ghost-FEM, a recent unfitted boundary method first introduced in [4, 6]. The same space discretization has been extended to the numerical solution of biological network formation in a leaf-shaped domain in [8] and to Multiscale Poisson-Nernst-Planck system [10, 3]. In [29], the authors present multigrid methods for solving elliptic partial differential equations on arbitrary domains using the same ghost-FEM discretization. In this method, a rectangular region discretized by a regular Cartesian mesh is arbitrarily intersected by the domain Ω . The active mesh Ω_h is the subset of the mesh that intersects Ω . The finite element method is based on a variational formulation over Ω_h , with stabilization terms to handle instabilities coming from small cut elements. In this study, the incompressible Navier-Stokes equations are solved in $\mathbb{Q}_2/\mathbb{Q}_1$ integrated FEM [31]. More importantly, the pressure variable is treated in a fully implicit manner, computing the solution of the pressure/velocity variables in a monolithic way.

Despite the abundance of unfitted finite element schemes available in the literature, such as CutFEM in [22] and AgFEM in [14, 12], the ghost-FEM is of interest for the following reason: when dealing with arbitrary domains, it is common to face small cut cells problem. While other schemes rely on stabilization techniques, the ghost-FEM employs a very simple algorithm based on snapping-back-to-grid approach to overcome the ill-conditioning issue, and it is straightforward to implement numerically. To the best of our knowledge, the use of IMEX schemes in conjunction with immersed boundary methods remains largely unexplored. Therefore, this work represents a significant contribution to this active area of research.

The paper is organized as follows. In Section 2, we present the mathematical model and its variational formulation. Section 3 describes the numerical tools employed in our simulations, starting from the level-set approach used to implicitly define the computational domain, the shifted boundary method adopted to handle geometric errors when prescribing boundary conditions on the approximated domain, the choice of the optimal penalization parameter for Dirichlet conditions, and the Aslam technique to extrapolate the solution outside the fluid domain. In Section 4, we first verify the expected order of accuracy in space and time of the proposed numerical scheme, and then present results for both steady and moving domains, including comparisons with established benchmark problems. We point out that the motion of the domain is assigned *a priori* (one-way coupling). Finally, we draw some conclusions.

2 Model and variational formulation

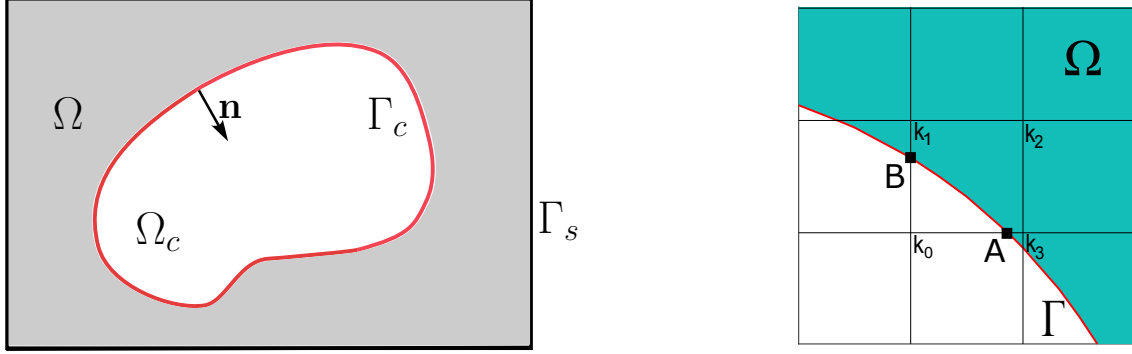
The incompressible Navier-Stokes equations are given by

$$\frac{\partial \mathbf{u}}{\partial t} + \mathbf{u} \cdot \nabla \mathbf{u} + \nabla p = \frac{1}{Re} \Delta \mathbf{u} + \mathbf{f} \quad \text{in } \Omega(t) \quad (1a)$$

$$\nabla \cdot \mathbf{u} = 0 \quad (1b)$$

$$\mathbf{u} = \mathbf{g} \quad \text{on } \Gamma, \quad (1c)$$

where $\mathbf{u} = \mathbf{u}(\mathbf{x}, t)$ is the fluid velocity, $p = p(\mathbf{x}, t)$ is the pressure, Re is the Reynolds number and $\mathbf{f} = \mathbf{f}(\mathbf{x}, t)$ the external forces. The domain $\Omega(t)$ is a bounded domain in \mathbb{R}^2 , and we assume that it is the difference between a fixed



(a) *Domain representation:* Ω is the domain, given as the difference between the rectangle R and Ω_c ; Γ_c is the internal boundary, for the computation of the points A and B . Γ_s the external squared boundary and \mathbf{n} the outer normal vector to Γ .

Figure 1: *Geometric features of the computational domain.*

rectangular region R of dimension $L_x \times L_y$ and a cavity $\Omega_c(t) \subseteq R$, that represents a solid object (see Fig. 1a). From now on, we omit the time dependence of the domain and of the boundary when it is clear from the context. We denote by $\Gamma_c = \partial\Omega_c$, $\Gamma_s = \partial R$, and $\Gamma = \partial\Omega$. Then, $\Gamma = \Gamma_c \cup \Gamma_s$. The system is closed by imposing Dirichlet boundary conditions on Γ . The governing equations are based on the fundamental physical principles of conservation and can be derived from the conservation of mass and momentum. Eq. (1a) represents the conservation of momentum, while Eq. (1b) is the incompressibility constraint forcing the conservation of mass. The main challenge in discretizing the system lies in the structure of the resulting algebraic problem. The saddle-point nature of the formulation, where the pressure acts as a Lagrange multiplier to enforce the incompressibility constraint, induces a coupling between velocity and pressure even at the discrete level [19, 15, 45]. In Section 3.1.3 we show the technique that we employ to deal with this feature.

Here we consider the variational formulation of Eqs. (1). We introduce the two spaces \mathbf{V} and Q defined as

$$\mathbf{V} = [H^1(\Omega)]^2, \quad Q = \left\{ q \in H^1(\Omega) : \int_{\Omega} q \, d\Omega = 0 \right\}. \quad (2)$$

Multiplying (1a) by a test function $\mathbf{w} \in \mathbf{V}$, (1b) by $q \in Q$, integrating over Ω and applying the divergence theorem, we obtain

$$\int_{\Omega} \frac{\partial \mathbf{u}}{\partial t} \cdot \mathbf{w} \, d\Omega + \int_{\Omega} (\mathbf{u} \cdot \nabla) \mathbf{u} \cdot \mathbf{w} \, d\Omega + \int_{\Omega} \nabla \mathbf{u} \cdot \nabla \mathbf{w} \, d\Omega - \int_{\Gamma} (\nabla \mathbf{u} \cdot \mathbf{n}) \cdot \mathbf{w} \, ds - \int_{\Gamma} \mathbf{u} \cdot (\nabla \mathbf{w} \cdot \mathbf{n}) \, ds \quad (3a)$$

$$+ \lambda \int_{\Gamma} \mathbf{u} \cdot \mathbf{w} \, ds - \int_{\Omega} p \nabla \cdot \mathbf{w} \, d\Omega + \int_{\Gamma} (p \mathbf{n}) \cdot \mathbf{w} \, ds = \int_{\Omega} f \cdot \mathbf{w} \, d\Omega + \lambda \int_{\Gamma} \mathbf{g} \cdot \mathbf{w} \, ds - \int_{\Gamma} \mathbf{g} \cdot (\nabla \mathbf{w} \cdot \mathbf{n}) \, ds \quad (3b)$$

$$\int_{\Omega} \nabla \cdot \mathbf{u} \, q \, d\Omega - \int_{\Gamma} (q \mathbf{n}) \cdot \mathbf{u} \, ds = - \int_{\Gamma} (q \mathbf{n}) \cdot \mathbf{g} \, ds. \quad (3c)$$

It is a well-established fact that as the penalization $\lambda \rightarrow \infty$ will force zero Dirichlet conditions [26, 27].

We denote by $(\cdot, \cdot)_{L^2(\Omega)}$ and $(\cdot, \cdot)_{L^2(\Gamma)}$ the scalar products in $L^2(\Omega)$ and $L^2(\Gamma)$, respectively. With this notation, the variational formulation of the problem reads as follows.

Problem 1. Given $\mathbf{f}, \mathbf{g} \in L^2(\Omega)$, find $\mathbf{u}(t) \in \mathbf{V}$ and $p(t) \in Q$, for almost every $t \in (0, T)$, such that

$$\begin{aligned} & \left(\frac{\partial \mathbf{u}}{\partial t}, \mathbf{w} \right)_{L^2(\Omega)} + ((\mathbf{u} \cdot \nabla) \mathbf{u}, \mathbf{w})_{L^2(\Omega)} + (\nabla \mathbf{u}, \nabla \mathbf{w})_{L^2(\Omega)} - (\nabla \mathbf{u} \cdot \mathbf{n}, \mathbf{w})_{L^2(\Gamma)} - (\mathbf{u}, \nabla \mathbf{w} \cdot \mathbf{n})_{L^2(\Gamma)} \\ & + \lambda(\mathbf{u}, \mathbf{w})_{L^2(\Gamma)} - (p, \nabla \cdot \mathbf{w})_{L^2(\Omega)} + (p \mathbf{n}, \mathbf{w})_{L^2(\Gamma)} = (\mathbf{f}, \mathbf{w})_{L^2(\Gamma)} + \lambda(\mathbf{g}, \mathbf{w})_{L^2(\Omega)} - (\mathbf{g}, \nabla \mathbf{w} \cdot \mathbf{n})_{L^2(\Gamma)} \quad \forall \mathbf{w} \in \mathbf{V} \\ & (\nabla \cdot \mathbf{u}, q)_{L^2(\Omega)} - (q \mathbf{n}, \mathbf{u})_{L^2(\Gamma)} = - (q \mathbf{n}, \mathbf{g})_{L^2(\Gamma)} \quad \forall q \in Q. \end{aligned}$$

2.1 Level-set representation of the domain

The domain Ω is implicitly defined by a level set function $\phi(x, y)$ such that [44, 48, 51, 53]:

$$\Omega = \{(x, y) : \phi(x, y) < 0\}, \quad \Gamma_c = \{(x, y) : \phi(x, y) = 0\}. \quad (5)$$

The unit normal vector on Γ_c pointing outward from Ω can be computed as

$$\mathbf{n} = \frac{\nabla \phi}{|\nabla \phi|}. \quad (6)$$

3 Numerical approximation

In this section, we describe the space and time discretization for the problem (1). For the spatial discretization, we follow the strategy in [4, 6], a recently developed ghost-FEM method. Time discretization is performed by an IMplicit EXplicit numerical scheme [16, Section 1.3], [38].

3.1 Spatial Discretization

The rectangular region $R = (x_{\min}, x_{\min} + L_x) \times (y_{\min}, y_{\min} + L_y)$ is discretized by a uniform mesh of squares (*cells*) of size $h = L_x/N_x = L_y/N_y$, where $N_x, N_y \in \mathbb{N}$ are the number of cells in x and y direction, respectively. The set of cells is denoted by \mathcal{C} , with $\#\mathcal{C} = N_x N_y$. A cell $K \in \mathcal{C}$ is classified as *active cell* if $K \cap \Omega \neq \emptyset$, or *inactive cell* otherwise. The union of all active cells is denoted by Ω_{act} . An active cell K can be *internal cell* if $K \subseteq \Omega$ or *cut cell* otherwise (namely $K \cap \Gamma \neq \emptyset$).

The discrete spaces \mathbf{V}_h and Q_h are constructed from continuous, piecewise polynomial functions defined on Ω_{act} . The functions \mathbf{w} and q , which are defined in the function spaces \mathbf{V} and Q , respectively, are approximated by the functions \mathbf{w}_h and q_h that belong to finite-dimensional subspaces \mathbf{V}_h and Q_h , defined as follows:

$$\mathbf{V}_h = \{\mathbf{v}_h \in \mathbf{V} : \mathbf{v}_h|_K \in [\mathbb{Q}_2(K)]^2, \quad \forall K \in \Omega_{\text{act}}\}, \quad (7a)$$

$$Q_h = \{q_h \in Q : q_h|_K \in \mathbb{Q}_1(K), \quad \forall K \in \Omega_{\text{act}}\}, \quad (7b)$$

where $\mathbb{Q}_1(K)$ and $\mathbb{Q}_2(K)$ denote, respectively, the spaces of bilinear and biquadratic Lagrangian shape functions on the element K . This choice of finite element spaces for the velocity/pressure fields is inf-sup stable [31], leading to third order accuracy for the velocity field and second order for the pressure.

In each cut cell, the portion of boundary is approximated by a straight line (see Algorithm 1 for more details). The union of these segments is denoted by Γ_h and the corresponding approximated domain by Ω_h . Consequently, the integrals in (1) defined over Ω and its boundary Γ are now evaluated over Ω_h and Γ_h , respectively, leading to the following discrete problem.

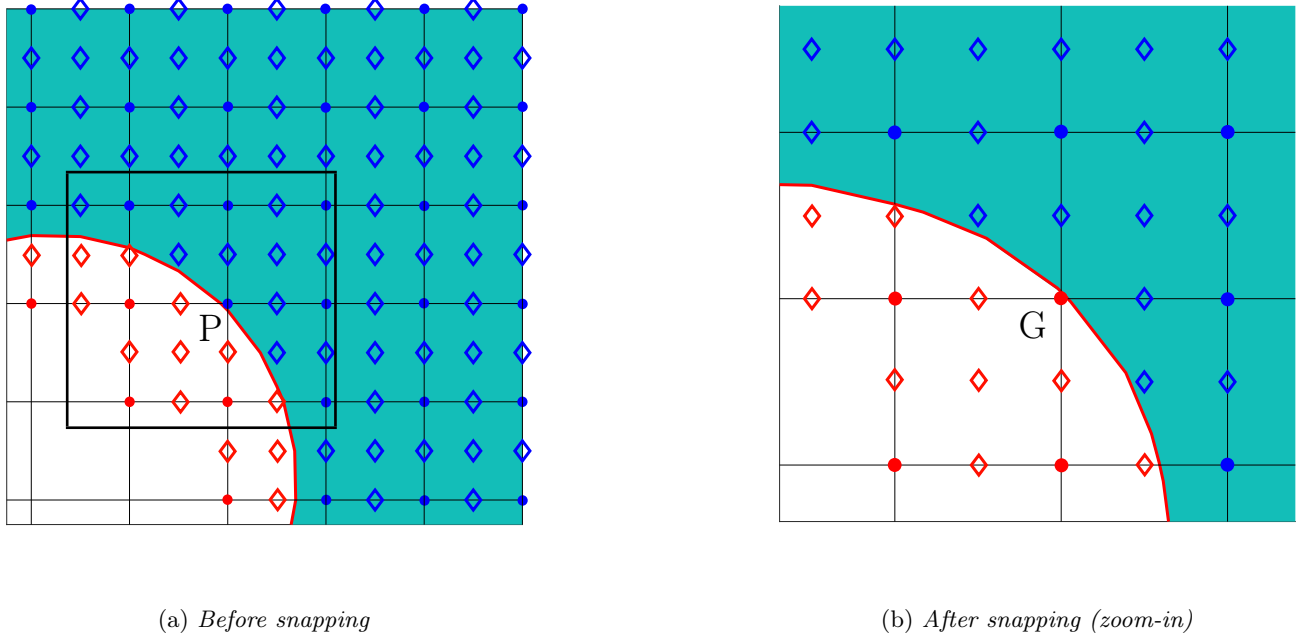


Figure 2: Classification of points and results of the snapping-back-to-grid algorithm. The internal point set \mathcal{I}_v is represented by blue dots and diamonds, while the set of \mathcal{I}_p is denoted by blue dots only. Red markers denote the respective sets of ghost points \mathcal{G}_v and \mathcal{G}_p . Panel (a) shows the grid before snapping, while panel (b) shows the grid after snapping. Panel (b) shows a zoom-in of the box highlighted in panel (a), where a point originally classified as internal, P , has changed its classification to ghost, G .

Problem 2. Given $\mathbf{f}_h, \mathbf{g}_h \in L^2(\Omega)$, find $\mathbf{u}_h \in \mathbf{V}_h$ and $p_h \in Q_h$ such that, for almost every $t \in (0, T)$, it holds

$$\left(\frac{\partial \mathbf{u}_h}{\partial t}, \mathbf{w}_h \right)_{L^2(\Omega_h)} + a_h(\mathbf{u}_h, \mathbf{w}_h) + b_h(p_h, \mathbf{w}_h) + c_h(\mathbf{u}_h, \mathbf{u}_h, \mathbf{w}_h) = (\mathbf{f}_h, \mathbf{w}_h)_{L^2(\Omega_h)} + \quad (8a)$$

$$+ \lambda(\mathbf{g}_h, \mathbf{w}_h)_{L^2(\Gamma_h)} - (\mathbf{g}_h, \nabla \mathbf{w}_h \cdot \mathbf{n})_{L^2(\Gamma_h)}, \quad \forall \mathbf{w}_h \in \mathbf{V}_h$$

$$b_h(q_h, \mathbf{u}_h) = (q_h \mathbf{n}, \mathbf{g}_h)_{L^2(\Gamma_h)}, \quad \forall q_h \in Q_h \quad (8b)$$

where

$$a_h(\mathbf{u}_h, \mathbf{w}_h) = (\nabla \mathbf{u}_h, \nabla \mathbf{w}_h)_{L^2(\Omega_h)} - (\nabla \mathbf{u}_h \cdot \mathbf{n}, \mathbf{w}_h)_{L^2(\Gamma_h)} - (\mathbf{u}_h, \nabla \mathbf{w}_h \cdot \mathbf{n})_{L^2(\Gamma_h)} + \lambda(\mathbf{u}_h, \mathbf{w}_h)_{L^2(\Gamma_h)} \quad (9a)$$

$$b_h(p_h, \mathbf{w}_h) = -(p_h, \nabla \cdot \mathbf{w}_h)_{L^2(\Omega_h)} + (p_h \mathbf{n}, \mathbf{w}_h)_{L^2(\Gamma_h)} \quad (9b)$$

$$c_h(\mathbf{v}_h, \mathbf{u}_h, \mathbf{w}_h) = ((\mathbf{v}_h \cdot \nabla) \mathbf{u}_h, \mathbf{w}_h)_{L^2(\Omega_h)}. \quad (9c)$$

We define bases for the spaces \mathbf{V}_h and Q_h . In particular, we first define two grids of nodes: \mathcal{N}_v and \mathcal{N}_p , as follows. The grid \mathcal{N}_v is constituted by the points $(x_{\min} + ih/2, y_{\min} + jh/2)$, for $i = 0, \dots, 2N_x$ and $j = 0, \dots, 2N_y$. The grid \mathcal{N}_p is constituted by the points $(x_{\min} + ih, y_{\min} + jh)$, for $i = 0, \dots, N_x$ and $j = 0, \dots, N_y$. Note that $\mathcal{N}_p \subset \mathcal{N}_v$ and that the closure of each cell K , denoted as \bar{K} , contains nine nodes of \mathcal{N}_v and four nodes of \mathcal{N}_p . For both grids, we define

the respective sets of active nodes \mathcal{A}_v and \mathcal{A}_p by $\mathcal{A}_{[v,p]} = \mathcal{N}_{[v,p]} \cap \Omega_{\text{act}}$. We partition active node sets into two subsets, respectively: $\mathcal{A}_{[v,p]} = \mathcal{I}_{[v,p]} \cup \mathcal{G}_{[v,p]}$, where $\mathcal{I}_{[v,p]}$ are the sets of internal nodes, and $\mathcal{G}_{[v,p]}$ are the sets of ghost nodes. We define them as follows: $\mathcal{I}_{[v,p]} = \mathcal{A}_{[v,p]} \cap \Omega$, $\mathcal{G}_{[v,p]} = \mathcal{A}_{[v,p]} \setminus \mathcal{I}_{[v,p]}$. In Fig. 2a, internal nodes of \mathcal{I}_v are depicted by blue markers, while the subset of active nodes of \mathcal{I}_p are the vertices of the cells and denoted by blue dots. Ghost points are denoted by red markers.

Let $D_{[v,p]} = |\mathcal{A}_{[v,p]}|$ be the cardinality of the respective active node sets. We observe that $\dim \mathbf{V}_h = 2D_v$ and $\dim Q_h = D_p$. We associate to each active node $\mathbf{x}_i \in \mathcal{A}_{[v,p]}$ a global shape function $\varphi_i^{[v,p]}$ uniquely defined by

$$\varphi_i^{[v,p]} \in \mathbb{Q}_{[2,1]}, \quad \text{supp } \varphi_i^{[v,p]} = \bigcup_{\bar{K} \ni \mathbf{x}_i} K, \quad \varphi_i^{[v,p]}(\mathbf{x}_j) = \delta_{ij}, \quad \forall \mathbf{x}_j \in \mathcal{A}_{[v,p]}.$$

The basis for \mathbf{V}_h is defined through shape functions $\{\varphi_1^v \mathbf{e}_1, \dots, \varphi_{D_v}^v \mathbf{e}_1, \varphi_1^v \mathbf{e}_2, \dots, \varphi_{D_v}^v \mathbf{e}_2\}$, where \mathbf{e}_1 and \mathbf{e}_2 are the vectors the canonical basis. Analogously, we define a basis for Q_h as $\{\varphi_i^p, i = 1, \dots, D_p\}$.

The discrete spaces are therefore

$$\mathbf{V}_h = \left\{ \mathbf{v}_h = v_h^1 \mathbf{e}_1 + v_h^2 \mathbf{e}_2, \quad v_h^{[1,2]} = \sum_{i=1}^{D_v} v_i^{[1,2]} \varphi_i^v \right\}, \quad Q_h = \left\{ q_h = \sum_{i=1}^{D_p} q_i \varphi_i^p \right\}.$$

We reformulate system (8) in a compact form, which will be used in the time discretization. To this end, we reuse (when it is clear from the context) the notation \mathbf{u}_h and p_h to denote the vectors of nodal values, that correspond to the components with respect to the bases introduced above. Introducing computational matrices representing the spatial derivatives, we obtain the following expression

$$\mathbb{M} \frac{\partial \mathbf{u}_h}{\partial t} = \mathbb{H}[\mathbf{u}_h] \mathbf{u}_h + \mathbb{G} p_h + \mathbb{M} (\mathbf{f}_h + \lambda \mathbf{g}_h) + \tilde{\mathbf{g}}_h \quad (10a)$$

$$\mathbb{G}^\top \mathbf{u}_h = \hat{\mathbf{g}}_h, \quad (10b)$$

where $\mathbb{M} = \begin{pmatrix} M & 0 \\ 0 & M \end{pmatrix}$, with $M_{ij} = (\varphi_i^v, \varphi_j^v)_{L^2(\Omega_h)}$ (the mass matrix), $\mathbb{H} = \begin{pmatrix} H^1[\mathbf{u}_h] & 0 \\ 0 & H^2[\mathbf{u}_h] \end{pmatrix}$, with $(H^{[1,2]}[\mathbf{u}_h])_{ij} = a_h(\varphi_i^v \mathbf{e}_{[1,2]}, \varphi_j^v \mathbf{e}_{[1,2]}) + c_h(\mathbf{u}_h, \varphi_i^v \mathbf{e}_{[1,2]}, \varphi_j^v \mathbf{e}_{[1,2]})$, $\mathbb{G} = \begin{pmatrix} G^1 \\ G^2 \end{pmatrix}$, with $G_{ij}^{[1,2]} = b_h(\varphi_j^p, \varphi_i^v \mathbf{e}_{[1,2]})$, $\tilde{\mathbf{g}}_h = \begin{pmatrix} \tilde{g}^1 \\ \tilde{g}^2 \end{pmatrix}$, with $\tilde{g}_i^{[1,2]} = (\mathbf{g}_h, \nabla \varphi_i^v \mathbf{e}_{[1,2]} \cdot \mathbf{n})_{L^2(\Gamma_h)}$, $(\hat{\mathbf{g}}_h)_i = (\varphi_i^p \mathbf{n}, \mathbf{g}_h)_{L^2(\Gamma_h)}$. We remind that these operators also include the boundary terms.

Eq. (10) can be summarized as follows

$$\mathbb{B} \frac{d\mathbf{q}_h}{dt} = \Theta[\mathbf{q}_h] \mathbf{q}_h + \bar{\mathbf{g}}_h, \quad (11)$$

where $\mathbf{q}_h = (\mathbf{u}_h, p_h)^\top$, and:

$$\mathbb{B} = \begin{pmatrix} \mathbb{M} & 0 \\ 0 & 0 \end{pmatrix}, \quad \Theta[\mathbf{q}_h] = \begin{pmatrix} \mathbb{H}[\mathbf{u}_h] & \mathbb{G} \\ \mathbb{G}^\top & 0 \end{pmatrix}, \quad \bar{\mathbf{g}}_h = \mathbb{B} (\mathbf{f}_h + \lambda \mathbf{g}_h) + \begin{pmatrix} \tilde{\mathbf{g}}_h \\ \hat{\mathbf{g}}_h \end{pmatrix}. \quad (12)$$

3.1.1 Geometrical error

In ghost-FEM, boundary conditions are not applied on the true boundary Γ but on an approximate one Γ_h , and it is essential to preserve the accuracy of their evaluation. To prevent any loss of accuracy that could degrade the overall convergence rates, we correct the boundary conditions via Taylor expansions, following the strategy proposed in the Shifted Boundary Method [11, 52]. We briefly describe the mentioned strategy.

Algorithm 1 Computation of the intersection of the boundary Γ with the grid (see Fig. 1b)

```

 $k_4 = k_0$ 
for  $i = 0:3$  do
  if  $\phi(k_i)\phi(k_{i+1}) < 0$  then
     $\theta = \phi(k_i)/(\phi(k_i) - \phi(k_{i+1}))$ 
     $P = \theta k_{i+1} + (1 - \theta)k_i$ 
    if  $\phi(k_i) < 0$  then
       $\mathbf{A} := P$ 
    else
       $\mathbf{B} := P$ 
    end if
  end if
end for

```

We first select a mapping between the real boundary Γ and the approximate one Γ_h , as follows

$$\mathcal{M}_h : \Gamma_h \rightarrow \Gamma$$

which maps any point $\mathbf{x} \in \Gamma_h$ to its orthogonal projection $\mathbf{z} = \mathcal{M}_h(\mathbf{x})$ on the physical boundary Γ . The projection point is computed via the Algorithm 2 (see [25, Sec. 3.1.2] for more details).

The mapping \mathcal{M}_h can be characterized through a distance vector function \mathbf{d} defined by

$$\mathbf{d}(\mathbf{x}) := \mathbf{z} - \mathbf{x} = (\mathcal{M}_h - I)(\mathbf{x}).$$

Let us assume that u is sufficiently smooth in the strip between Γ_h and Γ so that it admits a m -th order Taylor expansion, and let us denote by $\mathcal{D}_{\mathbf{d}}^i u = \sum_{\alpha \in \mathbb{N}^2, |\alpha|=i} \frac{i!}{\alpha!} \frac{\partial^i u}{\partial \mathbf{z}^\alpha} \mathbf{d}^\alpha$ the i -th order directional derivative along \mathbf{d} . Then, we can write

$$u(\mathbf{z}) = u(\mathbf{x} + \mathbf{d}(\mathbf{x})) = u(\mathbf{x}) + \sum_{i=1}^m \frac{\mathcal{D}_{\mathbf{d}}^i u(\mathbf{x})}{i!} + o(\|\mathbf{d}\|^m).$$

The Dirichlet boundary condition $u(\mathbf{z}) = g(\mathbf{z})$ on Γ is replaced by a boundary condition on Γ_h via

$$u(\mathbf{x}) = g(\mathcal{M}_h(\mathbf{x})), \quad \mathbf{x} \in \Gamma_h.$$

In this work, our aim is third-order accuracy, and therefore it suffices to set $m = 1$.

3.1.2 Choice of the penalization parameter and eigenvalue problem

We devote this section to discussing the choice of the penalization parameter λ in Eq. (8a). In [4], it was shown that setting $\lambda = ch^\alpha$ with $c \in \mathbb{R}$ sufficiently large, and $\alpha = 2$ ensures well-posedness for the Poisson's problem. In the present work, we extend this analysis to time-dependent problems and higher-order discretizations. Let $c_0 > 0$ be a constant such that the bilinear form is coercive. Then, for any $c > c_0$, the formulation is well-posed. However, combined with IMEX, the choice of this constant is crucial: in some cases, when the penalization parameter is too small, it can lead to a loss of stability in the discretization, while large values result in severe ill-conditioning of the linear system. The selection of the stabilization parameter is therefore critical and several approaches for estimating this parameter are based on solving general eigenvalue problems [35, 30, 34].

Algorithm 2 Computation of the projection point $\mathbf{z} = \mathcal{M}_h(\mathbf{x})$

```

toll = 10-2h2
ε = h/10
k = 0
Δ = 2 toll
 $\mathbf{x}^{(0)} = \mathbf{x}$ 
while Δ > toll do
   $\mathbf{a}^{(k)} = -\epsilon\phi(\mathbf{x}^{(k)}) \frac{\nabla\phi(\mathbf{x}^{(k)})}{|\nabla\phi(\mathbf{x}^{(k)})|^2}$ 
   $\mathbf{x}^{(k+1)} = \mathbf{x}^{(k)} + \mathbf{a}^{(k)}$ 
  Δ =  $\|\mathbf{x}^{(k+1)} - \mathbf{x}^{(k)}\|$ 
  k = k + 1
end while
 $\mathbf{z} = \mathbf{x}^{(k)}$ 

```

The bilinear form in Eq. (8) is coercive if there exists a positive constant $\tilde{C} > 0$ such that $a_h(\mathbf{u}_h, \mathbf{u}_h) \geq \tilde{C}\|\mathbf{u}_h\|_{\mathbf{V}_h}$ for any $\mathbf{u}_h \in \mathbf{V}_h$. Here, the norm on the FE space \mathbf{V}_h is defined as

$$\|\mathbf{u}_h\|_{\mathbf{V}_h}^2 = \|\nabla\mathbf{u}_h\|_{L^2(\Omega_h)}^2 + \lambda\|\mathbf{u}_h\|_{L^2(\Gamma_h)}^2. \quad (13)$$

To establish a lower bound on the bilinear form $a_h(\mathbf{u}_h, \mathbf{u}_h)$, we use the strategy of [49], as described below. We apply Young's inequality, which states that for any two real numbers a and b and a positive parameter ε we have $ab \leq a^2/(2\varepsilon) + \varepsilon b^2/2$. Applying it to the boundary integral term, we obtain:

$$\int_{\Gamma_h} 2\mathbf{u}_h(\mathbf{n} \cdot \nabla\mathbf{u}_h)ds \leq \frac{1}{\varepsilon} \int_{\Gamma_h} \mathbf{u}_h\mathbf{u}_h ds + \varepsilon \int_{\Gamma_h} (\mathbf{n} \cdot \nabla\mathbf{u}_h)(\mathbf{n} \cdot \nabla\mathbf{u}_h)ds.$$

Therefore:

$$\begin{aligned} a_h(\mathbf{u}_h, \mathbf{u}_h) &= \int_{\Omega_h} \nabla\mathbf{u}_h \cdot \nabla\mathbf{u}_h d\Omega + \int_{\Gamma_h} \lambda\mathbf{u}_h\mathbf{u}_h - 2\mathbf{u}_h(\mathbf{n} \cdot \nabla\mathbf{u}_h)ds \\ &\geq \int_{\Omega_h} \nabla\mathbf{u}_h \cdot \nabla\mathbf{u}_h d\Omega - \varepsilon \int_{\Gamma_h} (\mathbf{n} \cdot \nabla\mathbf{u}_h)(\mathbf{n} \cdot \nabla\mathbf{u}_h)ds + \left(\lambda - \frac{1}{\varepsilon}\right) \int_{\Gamma_h} \mathbf{u}_h\mathbf{u}_h ds \\ &\geq (1 - C\varepsilon) \int_{\Omega_h} \nabla\mathbf{u}_h \cdot \nabla\mathbf{u}_h d\Omega + \left(\lambda - \frac{1}{\varepsilon}\right) \int_{\Gamma_h} \mathbf{u}_h\mathbf{u}_h ds, \end{aligned}$$

where in the last expression we assume that there exists a constant $C > 0$ such that

$$C \int_{\Omega_h} \nabla\mathbf{u}_h \cdot \nabla\mathbf{u}_h d\Omega \geq \int_{\Gamma_h} (\mathbf{n} \cdot \nabla\mathbf{u}_h)(\mathbf{n} \cdot \nabla\mathbf{u}_h)ds. \quad (14)$$

The bilinear form is coercive if $1 - C\varepsilon > 0$ and $\lambda - \frac{1}{\varepsilon} > 0$. Hence, a necessary condition for the stabilization parameter is $\lambda > C$.

The first step is to find an estimate for the smallest value of C such that (14) is satisfied. This is obtained by solving the generalized global eigenvalue problem

$$\mathbf{K}v = \Lambda\mathbf{M}v, \quad (15)$$

where $\mathbf{K}_{ij} = \int_{\Gamma_h} (\mathbf{n} \cdot \nabla\varphi_i^v)(\mathbf{n} \cdot \nabla\varphi_j^v) ds$ and $\mathbf{M}_{ij} = \int_{\Omega_h} \nabla\varphi_i^v \cdot \nabla\varphi_j^v d\Omega$ for $i, j \in \{1, 2, \dots, D^v\}$. The lower bound of C is then estimated by taking $C = \max \Lambda$. The stabilization parameter is then chosen as $\lambda = \gamma C$, for some constant $\gamma > 1$ (we used $\gamma = 1.1$ in our tests).

3.1.3 Stabilization technique for the saddle-point problem

The discretization of the pressure term may introduce instabilities, as the pressure appears only in the form of its gradient, resulting in a non-unique solution of the problem 12. In finite difference schemes, this issue can be addressed by employing a mixed interpolation strategy based on the MAC grid [40, 24]. Analogously, when using finite element methods, a mixed formulation is adopted [15].

In Section 3.2, we will employ a semi-implicit time discretization, then a linear system will be solved at each time step. The matrix of the linear system will take the form

$$\mathbb{B} - k\Delta t \Theta[\mathbf{q}_h],$$

for some $k \in \mathbb{R}$ that depends on the choice of the IMEX scheme (a detailed explanation is given in Section 3.2.) The singularity of the matrix $\mathbb{B} - k\Delta t \Theta[\mathbf{q}_h]$ is addressed by introducing a stabilization diagonal submatrix to $\Theta[\mathbf{q}_h]$ as follows

$$\Theta[\mathbf{q}_h] = \begin{pmatrix} \mathbb{H}[\mathbf{u}_h] & \mathbb{G} \\ \mathbb{G}^\top & \varepsilon \mathbb{I} \end{pmatrix}. \quad (16)$$

We set $\varepsilon = 10^{-10}$ in our numerical simulations.

3.2 Temporal discretization

In this section we describe the time discretization strategy to solve Eq. (11). We adopt an IMEX scheme, which offers a flexible framework to obtain arbitrary order of accuracy.

We consider a final time T and define the time step size as $\Delta t = T/N_{\text{ts}}$, $N_{\text{ts}} \in \mathbb{N}$, denoting the time steps by $t^n = n\Delta t$ and $\mathbf{q}^n \approx \mathbf{q}(t^n)$, $n = 0, \dots, N_{\text{ts}}$.

Observe that vector $\bar{\mathbf{g}}_h$ of Eq. (11) may depend on time (for example, when source terms and boundary conditions are time dependent), then we write $\bar{\mathbf{g}}_h(t)$.

We first set $\mathbf{q}_E^1 = \mathbf{q}^n$, then the stage fluxes \mathbf{q}_E^i and \mathbf{q}_I^i are calculated as

$$\mathbb{B} \mathbf{q}_E^i = \mathbb{B} \mathbf{q}^n + \Delta t \sum_{j=1}^{i-1} \tilde{a}_{i,j} \left(\Theta[\mathbf{q}_E^j] \mathbf{q}_I^j + \bar{\mathbf{g}}_h(t^n + \tilde{c}_j \Delta t) \right), \quad (17a)$$

$$\mathbb{B} \mathbf{q}_I^i = \mathbb{B} \mathbf{q}^n + \Delta t \sum_{j=1}^i a_{i,j} \left(\Theta[\mathbf{q}_E^j] \mathbf{q}_I^j + \bar{\mathbf{g}}_h(t^n + c_j \Delta t) \right), \quad (17b)$$

for $i = 1, \dots, s$, where s is the number of stages of the scheme. The numerical solution is finally updated with

$$\mathbb{B} \mathbf{q}^{n+1} = \mathbb{B} \mathbf{q}^n + \Delta t \sum_{i=1}^s \left(\tilde{b}_i (\Theta[\mathbf{q}_E^i] \mathbf{q}_I^i + \bar{\mathbf{g}}_h(t^n + \tilde{c}_i \Delta t)) + b_i (\Theta[\mathbf{q}_E^i] \mathbf{q}_I^i + \bar{\mathbf{g}}_h(t^n + c_i \Delta t)) \right). \quad (18)$$

The coefficients $\tilde{a}_{i,j}$, $a_{i,j}$, \tilde{c}_i , c_i , \tilde{b}_i , b_i are taken from double Butcher tableaux

$$\begin{array}{c|c} \tilde{c} & \tilde{A} \\ \hline & \tilde{b} \end{array} \quad \begin{array}{c|c} c & A \\ \hline & b \end{array}$$

In our numerical tests we choose $s = 2$ or $s = 4$ for a second or third order accuracy, respectively, and adopt the following Butcher tableaux [16].

Two-stage second-order IMEX scheme

For a second-order numerical scheme ($s = 2$):

$$\begin{array}{c|cc} 0 & 0 & 0 \\ 1 & 1 & 0 \\ \hline & 1/2 & 1/2 \end{array} \quad \begin{array}{c|cc} 1-\eta & 1-\eta & 0 \\ \eta & \eta-\delta & \delta \\ \hline & 1/2 & 1/2 \end{array}$$

with $\eta = 1/\sqrt{2}$ and $\delta = 1 - 1/(2\eta)$.

Four-stage third-order IMEX scheme

For a third-order numerical scheme ($s = 4$):

$$\begin{array}{c|cccc} 0 & 0 & 0 & 0 & 0 \\ \gamma & \gamma & 0 & 0 & 0 \\ 0.717933260754 & 1.243893189 & -0.5259599287 & 0 & 0 \\ 1 & 0.6304125582 & 0.7865807402 & -0.4169932983 & 0 \\ \hline & 0 & 1.208496649176 & -0.644363170684 & \gamma \\ \\ \gamma & \gamma & 0 & 0 & 0 \\ \gamma & 0 & \gamma & 0 & 0 \\ 0.717933260754 & 0 & 0.282066739245 & \gamma & 0 \\ 1 & 0 & 1.208496649176 & -0.644363170684 & \gamma \\ \hline & 0 & 1.208496649176 & -0.644363170684 & \gamma \end{array}$$

with $\gamma = 0.435866521508$.

3.2.1 Extrapolation technique and moving domains

When dealing with moving domains, we need a strategy to extrapolate functions beyond the current domain. In order to solve Eqs. (17) and (18) on $\Omega_{\text{act}}^{n+1}$, we need to extend \mathbf{q}^n , originally defined on Ω_{act}^n , to the active nodes of $\Omega_{\text{act}}^{n+1}$ not contained in Ω_{act}^n . We remark that the motion of the domain is prescribed *a priori* (one-way coupling).

Here, we adapt the strategy proposed in [2] for finite difference schemes to the finite element framework. In Algorithm 3 we show how to obtain a quadratic extrapolation (to achieve third order accuracy) of a function u .

We start defining the characteristic function of $\Omega_{\text{com}}^n := R \setminus \Omega_{\text{act}}^n$, as

$$\chi(\mathbf{x}) = \begin{cases} 0 & \text{if } \mathbf{x} \in \Omega_{\text{act}}^n, \\ 1 & \text{otherwise.} \end{cases} \quad (19)$$

Making use of it, we preserve the values of the solution at the nodes of Ω_{act}^n (active nodes), while evolving the function in Ω_{com}^n , according to the Algorithm 3.

Algorithm 3 Quadratic extrapolation of a function u to Ω_{com}^n . Eqs (20), (21) and (22) are solved in a fictitious time τ up to steady-state in a narrow boundary layer.

Compute $u_{\mathbf{n}} := \mathbf{n} \cdot \nabla u$
 Compute $u_{\mathbf{nn}} := \mathbf{n} \cdot \nabla u_{\mathbf{n}}$
 Solve

$$\frac{\partial u_{\mathbf{nn}}}{\partial \tau} + \chi \mathbf{n} \cdot \nabla u_{\mathbf{nn}} = 0 \quad (20)$$

Solve

$$\frac{\partial u_{\mathbf{n}}}{\partial \tau} + \chi (\mathbf{n} \cdot \nabla u_{\mathbf{n}} - u_{\mathbf{nn}}) = 0 \quad (21)$$

Solve

$$\frac{\partial u}{\partial \tau} + \chi (\mathbf{n} \cdot \nabla u - u_{\mathbf{n}}) = 0 \quad (22)$$

The strategy of Algorithm 3 is as follows: the Heaviside function ensures that the known values of our function remain unchanged in Ω_{act}^n . In the region Ω_{com}^n , Eq. (20) defines a linear hyperbolic PDE with characteristics along \mathbf{n} ; we solve it until we reach steady-state in a narrow boundary layer of width $3h$, where we have $\mathbf{n} \cdot \nabla u_{\mathbf{nn}} = 0$, meaning that $u_{\mathbf{nn}}$ is constant along the characteristic direction. Once the second directional derivative $u_{\mathbf{nn}}$ is available in boundary layer from Eq. (20), we first recover the first directional derivative $u_{\mathbf{n}}$ using Eq. (21), and then proceed with a second integration step in Eq. (22) to obtain the extrapolated solution u . The extrapolated solution retains the order of accuracy, corresponding to the order of extrapolation, only within the prescribed narrow band near the boundary. Solutions obtained using quadratic extrapolation for various geometries are shown in Figure 3. In our numerical simulations, we extrapolate the solutions in a band of width $3h$, while the extrapolated solutions in Figure 3 are displayed in a region larger than this band, for graphical purposes. However, when a wider region is considered, central differences are not stable and one has to use upwind discretization to get a smooth extrapolation. We show in Fig. 4 the extrapolated solution in a wider layer by using upwind discretization of the convective term.

To solve Eqs. (20-22), we first consider the variational formulation of the respective equations. As we did in Section 2, multiplying (20-22) by a test function $\mathbf{w} \in \mathbf{V}$ and integrating over Ω , we obtain the following system

$$\begin{aligned} \int_{\Omega} \left(\frac{\partial u_{\mathbf{nn}}}{\partial \tau} + \chi \mathbf{n} \cdot \nabla u_{\mathbf{nn}} \right) \mathbf{w} \, d\Omega &= 0 \\ \int_{\Omega} \left(\frac{\partial u_{\mathbf{n}}}{\partial \tau} + \chi (\mathbf{n} \cdot \nabla u_{\mathbf{n}} - u_{\mathbf{nn}}) \right) \mathbf{w} \, d\Omega &= 0 \\ \int_{\Omega} \left(\frac{\partial u}{\partial \tau} + \chi (\mathbf{n} \cdot \nabla u - u_{\mathbf{n}}) \right) \mathbf{w} \, d\Omega &= 0 \end{aligned}$$

Analogously to variational formulation introduced in (1), the integrals defined over Ω are then evaluated in Ω_h .

4 Numerical results

In this section, we test our numerical schemes. We begin with simulations on a stationary domain. Subsequently, we present numerical results in the context of moving domains.

All numerical experiments have been implemented using `Gridap` (version 0.17.23), a Julia-based open-source software designed for approximating the solution of PDEs [13]. `Gridap` leverages the Julia JIT (just-in-time) compiler and has a

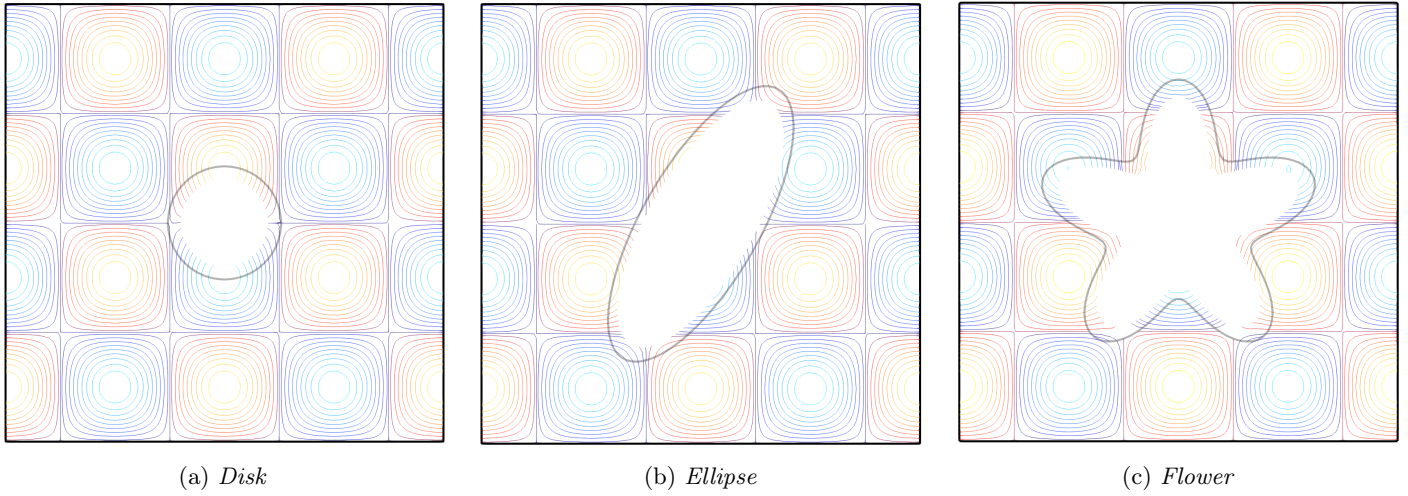


Figure 3: *Plot of extrapolated solutions using quadratic extrapolation on a narrow band near the boundary for different geometries.*

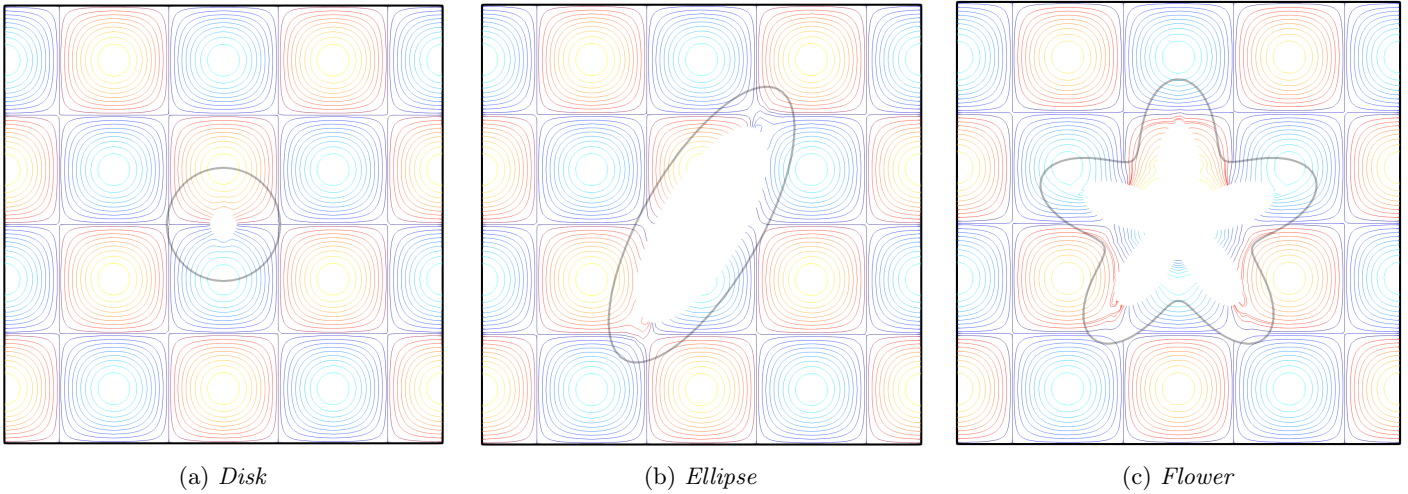


Figure 4: *Plot of extrapolated solutions using quadratic extrapolation on a wider band near the boundary for different geometries, using upwind discretization for the convective term.*

user-interface that closely resembles that whiteboard-style notation of the weak formulation [60]. In particular, we used GridapEmbedded (version 0.9.5) [61], a plug-in that provides tools for implementing embedded finite element methods.

4.1 Accuracy tests: Stationary domain

In this section, we consider a time independent domain, i.e. $\Omega(t) = \Omega$. We consider the Kim and Moin problem, for which an exact solution is available. Let us consider the square region $R = [-1, 1]^2$ and the Navier-Stokes problem with Dirichlet conditions, whose exact solution is

$$u^{\text{exa}} = \sin(2\pi x) \cos(2\pi y) e^{(-2\nu t)} \quad (23a)$$

$$v^{\text{exa}} = -\cos(2\pi x) \sin(2\pi y) e^{(-2\nu t)} \quad (23b)$$

$$p^{\text{exa}} = -0.25 (\cos(4\pi x) + \cos(4\pi y)) e^{(-4\nu t)} \quad (23c)$$

We take $\nu = 1$, corresponding to $Re = 1$. The domains we consider are defined by the following level set function (see Fig. 5) :

(a) Disk:

$$\phi(x, y) = \frac{1}{\sqrt{15}} - \sqrt{x^2 + y^2} \quad (24)$$

(b) Ellipse:

$$A = \frac{1}{\sqrt{14}}, \quad B = \frac{1}{\sqrt{2}}, \quad \theta = \frac{\pi}{6}, \quad (25)$$

$$\phi(x, y) = 1 - \frac{(\cos(\theta)x - \sin(\theta)y)^2}{A^2} - \frac{(\sin(\theta)x + \cos(\theta)y)^2}{B^2} \quad (26)$$

(c) Flower:

$$A = 0.5, \quad B = 0.15, \quad R = \sqrt{x^2 + y^2}, \quad (27)$$

$$\phi(x, y) = A - R + \frac{B(y^5 + 5x^4y - 10x^2y^3)}{R^5} \quad (28)$$

In Fig. 6, we show the plot of relative errors against spatial mesh size h for various stationary geometries, choosing the two-step IMEX scheme. The time step size is chosen as $\Delta t = h$. The following quantities are computed and plotted:

$$\begin{aligned} \text{Total } L^2 \text{ error} &= \frac{\left(\sum_{n=h=1}^{N_{ts}} \|\mathbf{u}_{exa}(t^n) - \mathbf{u}_h^n\|_{L^2(\Omega_h)}^2 \right)^{1/2}}{\left(\sum_{n=1}^{N_{ts}} \|\mathbf{u}_{exa}(t^n)\|_{L^2(\Omega_h)}^2 \right)^{1/2}}, & \text{Total } H^1 \text{ error} &= \frac{\left(\sum_{n=1}^{N_{ts}} \|\mathbf{u}_{exa}(t^n) - \mathbf{u}_h^n\|_{H^1(\Omega_h)}^2 \right)^{1/2}}{\left(\sum_{n=1}^{N_{ts}} \|\mathbf{u}_{exa}(t^n)\|_{H^1(\Omega_h)}^2 \right)^{1/2}}, \\ L^2 \text{ error at final time} &= \frac{\|\mathbf{u}_{exa}(t^{N_{ts}}) - \mathbf{u}_h^{N_{ts}}\|_{L^2(\Omega_h)}}{\|\mathbf{u}_{exa}(t^{N_{ts}})\|_{L^2(\Omega_h)}}, & H^1 \text{ error at final time} &= \frac{\|\mathbf{u}_{exa}(t^{N_{ts}}) - \mathbf{u}_h^{N_{ts}}\|_{H^1(\Omega_h)}}{\|\mathbf{u}_{exa}(t^{N_{ts}})\|_{H^1(\Omega_h)}}, \end{aligned}$$

where $\|u\|_{L^2(\Omega_h)}^2 = \int_{\Omega_h} (u \cdot u) d\Omega$ and $\|u\|_{H^1(\Omega_h)}^2 = \|u\|_{L^2(\Omega_h)}^2 + \int_{\Omega_h} (\nabla u \cdot \nabla u) d\Omega$. We observe from Fig. 6 that the final-time errors are indistinguishable from the total ones, meaning that the scheme is stable over time. Therefore, for all the following tests we show only the total errors (in L^2 and H^1 norms). In Fig. 7, we repeat the same test, using the four-step IMEX scheme. For this choice of IMEX scheme, we set $\Delta t = h/2$. As shown in Fig. 6, the accuracy tests on

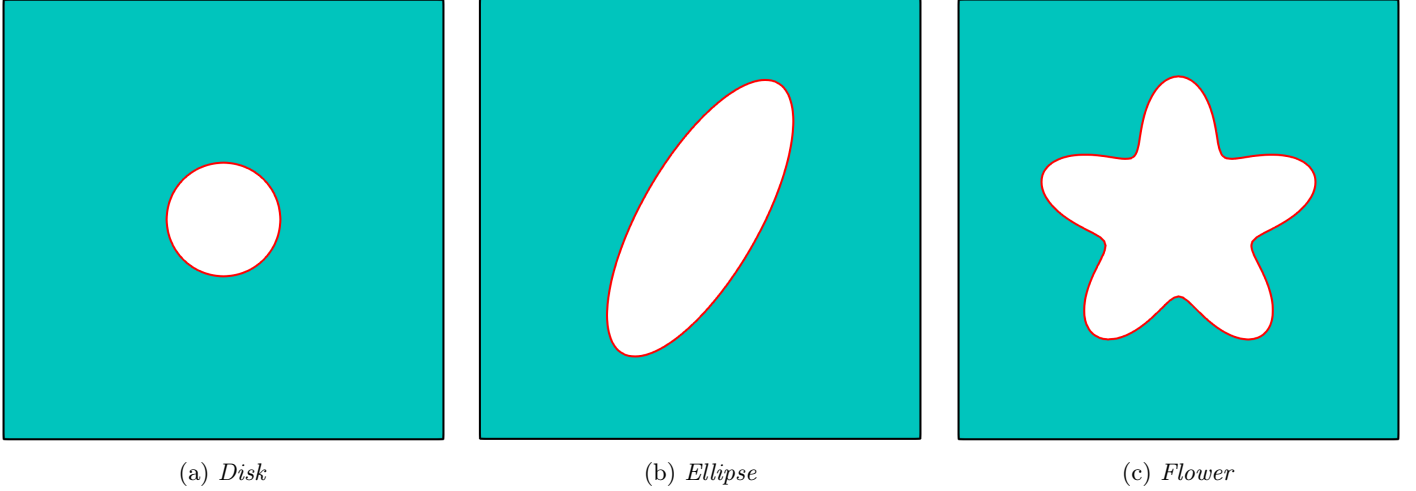


Figure 5: *Geometries used for tests.*

stationary domains indicate that, for the two-stage second-order IMEX scheme, both the L^2 and H^1 errors decrease with a rate of 2, consistent with theoretical expectations. As shown in Fig. 7, for the four-stage third-order IMEX scheme on stationary domains, the L^2 error exhibits third-order convergence, while the H^1 error converges at second order, as expected. Overall, these results confirm that the numerical schemes achieve their expected orders of accuracy.

4.2 Accuracy tests: Moving domain

In this section, we perform numerical tests on domains that depend on time. The evolution of the moving domain is defined by time-dependent level set function $\phi(x, y, t) = \phi_0(\tilde{x}(t), \tilde{y}(t))$, where $\phi_0(x, y)$ represents the domain at time $t = 0$, and

$$\begin{pmatrix} \tilde{x}(t) \\ \tilde{y}(t) \end{pmatrix} = \begin{pmatrix} \cos(\omega t) & -\sin(\omega t) \\ \sin(\omega t) & \cos(\omega t) \end{pmatrix} \begin{pmatrix} x \\ y \end{pmatrix}, \quad (29)$$

with an angular velocity of $\omega = 2\pi/5$. We test rotating ellipse and flower, then the initial level set $\phi_0(x, y)$ is given by Eq. (25) (ellipse) or Eq. (27) (flower).

Relative errors against spatial mesh sizes h are illustrated in Fig. 8. The four-step IMEX scheme attains third-order convergence in the L^2 norm and second-order convergence in the H^1 norm, in agreement with theoretical expectations, even on moving geometries.

4.3 Flow around a disk

In this test, we study the unsteady two-dimensional flow around a circular disk at Reynolds number $Re = 100$ [50]. The computational domain is given by $\Omega = [0, 2.2] \times [0, 0.41] \setminus B_R$, where B_R is a disk centered at $(0.2, 0.2)$ with radius $R_B = 0.05$. No-slip boundary conditions are imposed on the lower and upper walls $\Gamma_1 = [0, 2.2] \times \{0\}$ and $\Gamma_2 = [0, 2.2] \times \{0.41\}$ as well as on the boundary of the disk $\Gamma_3 = \partial B_R$, that is

$$\mathbf{u}|_{\Gamma_1} = \mathbf{u}|_{\Gamma_2} = \mathbf{u}|_{\Gamma_3} = \mathbf{0}.$$

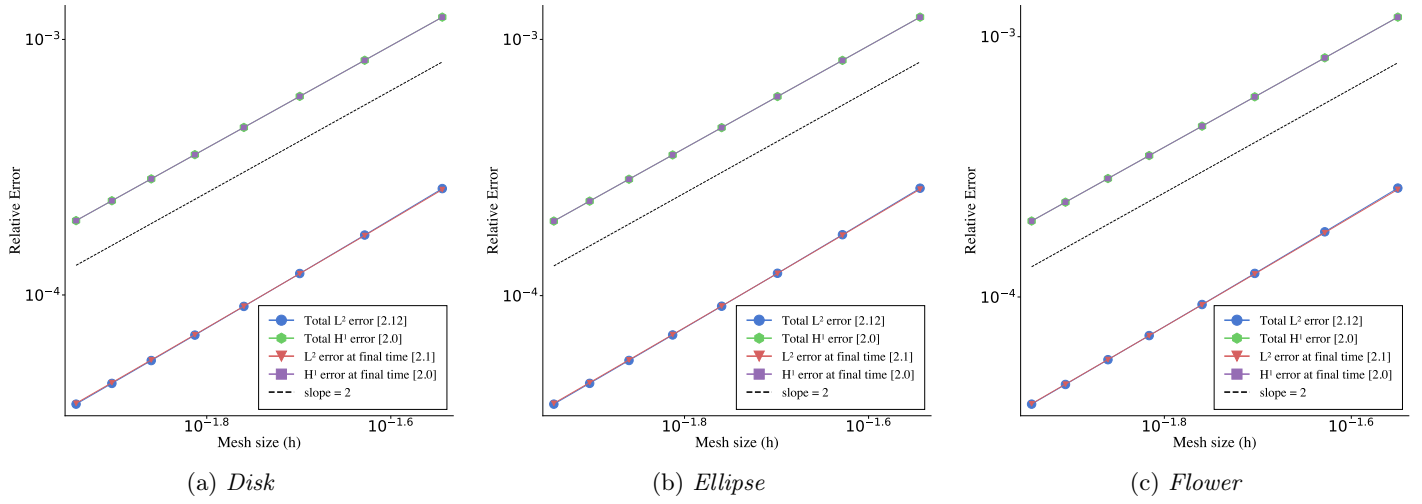


Figure 6: Plots of relative errors against spatial mesh size h for a two-stage second-order IMEX scheme for Navier-Stokes equations on various stationary geometries.

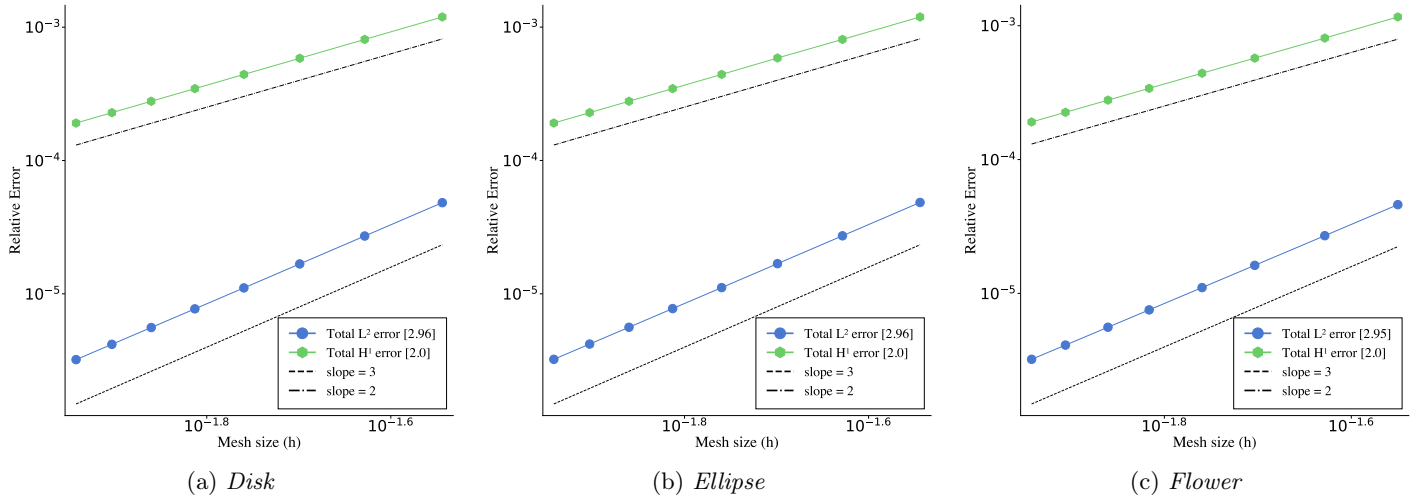
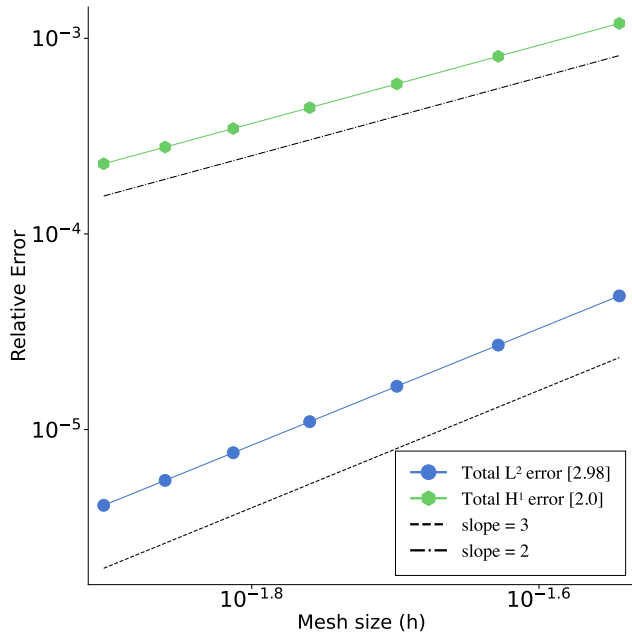
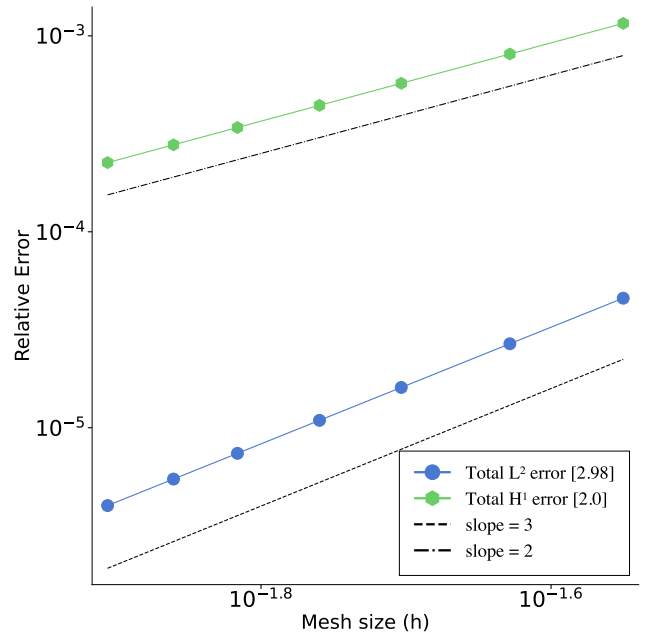


Figure 7: Plots of relative errors against spatial mesh size h for a four-stage third-order IMEX scheme for Navier-Stokes equations on different stationary geometries.



(a) *Ellipse*



(b) *Flower*

Figure 8: *Plots of relative errors against spatial mesh size h for a four-stage third-order IMEX scheme for Navier-Stokes equations on different moving geometries.*

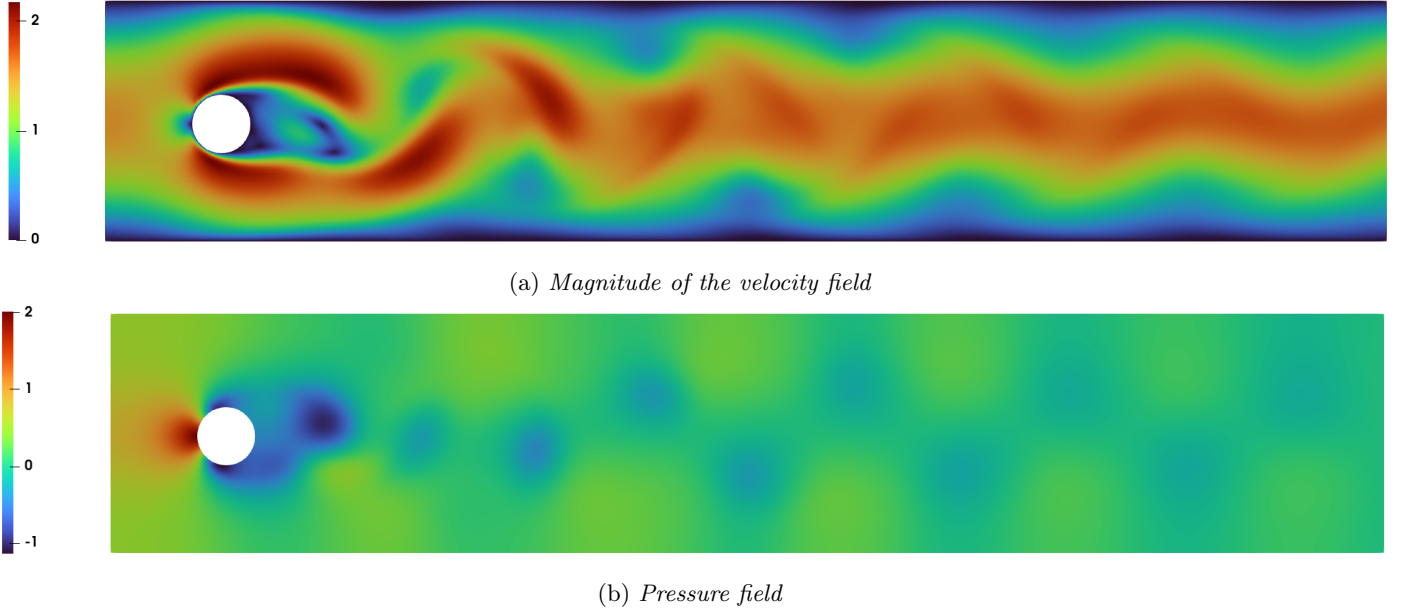


Figure 9: *The magnitude of the velocity and pressure fields for flow around a disk at time = 10s for $Re = 100$.*

On the inlet $\Gamma_4 = \{0\} \times [0, 0.41]$, a parabolic inflow is prescribed as $\mathbf{u}(0, y) = \left(\frac{4Uy(0.41-y)}{0.41^2}, 0 \right)$, where $U = 1.5$ denotes the maximum inflow velocity. At the outlet $\Gamma_5 = \{2.2\} \times [0, 0.41]$, the do-nothing boundary condition is applied $\nu \partial_{\mathbf{n}} \mathbf{u} - p \mathbf{n} = 0$, where \mathbf{n} denotes the outward normal. Following [50] $\nu = 0.001$, $Re = \frac{2}{3} u(0, 0.41/2) (2R_B) / \nu$. The final simulation time is set to $T = 10s$, with a time step $\Delta t = 0.01s$. The velocity and pressure fields at the final time are shown in Fig. 9. The results exhibit the formation of alternating vortices in the wake of the cylinder, which is consistent with the expected behavior at $Re = 100$.

The drag and lift forces on the cylinder are computed as

$$(F_D, F_L) = \int_{\Gamma_3} (\nu \nabla \mathbf{u} - p \mathbf{I}) \mathbf{n} \, d\mathbf{S},$$

where \mathbf{n} denotes the outward unit normal on the disk boundary Γ_3 . The drag and lift coefficients are defined as

$$C_D = \frac{2}{U_{\text{mean}}^2 L} F_D, \quad C_L = \frac{2}{U_{\text{mean}}^2 L} F_L,$$

where $U_{\text{mean}} = 1$ is the mean velocity of the parabolic inflow velocity and $L = 2r = 0.1$ is the characteristic length of the flow configuration.

The following quantities are computed: the drag coefficient C_D , the lift coefficient C_L , and the pressure difference ΔP as functions of time over one period $[t_0, t_0 + 1/f]$, where $f = f(C_L)$ denotes the frequency of the lift coefficient; the maximum drag coefficient $C_{D,\text{max}}$ and the maximum lift coefficient $C_{L,\text{max}}$; the Strouhal number St ; the pressure difference $\Delta p(t)$ evaluated at $t = t_0 + \frac{1}{2f}$. The initial data at $t = t_0$ corresponds to a flow state with $C_{L,\text{max}}$. The numerical measured quantities are presented in Tab. 1. Fig. 10 depicts the drag and lift coefficients as well as the pressure difference $\Delta p = p(a_1) - p(a_2)$ between the points $a_1 = (0.15, 0.2)$ on the front of the disk and $a_2 = (0.25, 0.2)$ on the rear of the disk over the interval $[t_0, t_0 + 1/f]$.

Quantity	# Elements	# Unknowns	$C_{D,\max}$	$C_{L,\max}$	St	Δp
Reference value			3.22 - 3.24	0.99 - 1.01	0.295 - 0.305	2.46 - 2.50
Measured value	11668	104407	3.20227	1.00773	0.30303	2.50133

Table 1: Numerically measured quantities for a flow past a disk

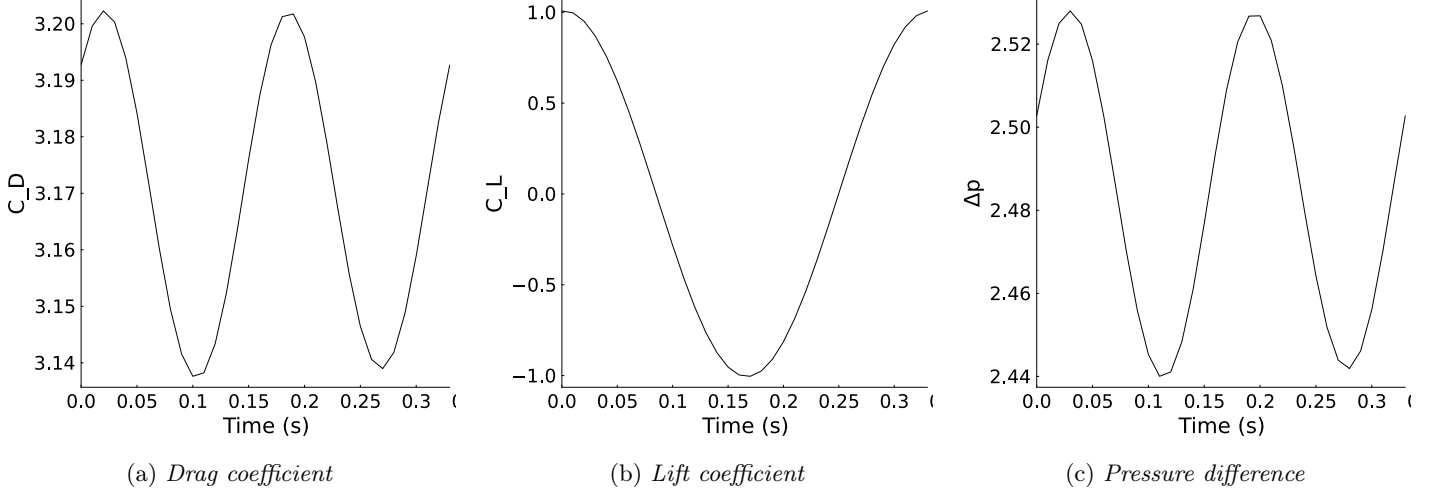


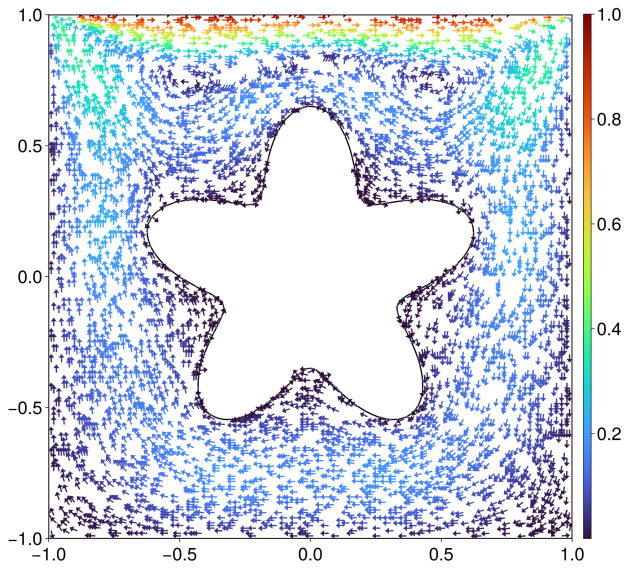
Figure 10: Plots of the measured numerical quantities over the time interval $[t_0, t_0 + 1/f]$ for a flow around a disk.

The numerically measured results are in good agreement with the reference ranges for the flow past a disk taken from [50], and the periodic drag and lift coefficients as well as the pressure difference exhibit stable amplitudes, confirming that the simulation accurately captures the unsteady flow dynamics.

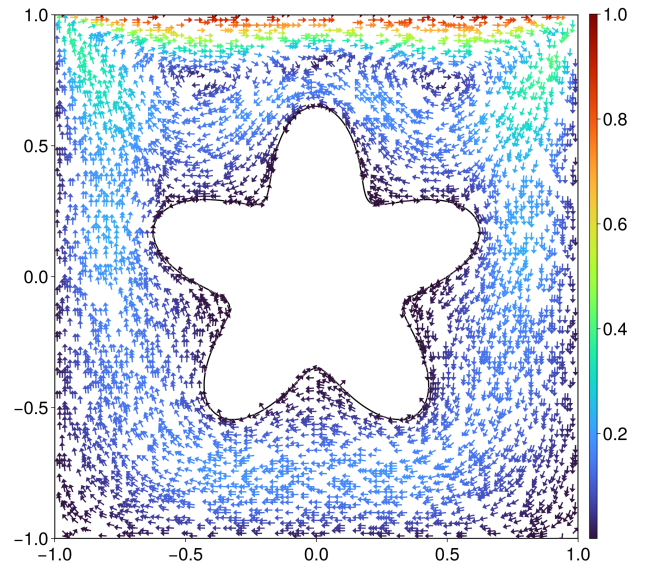
4.4 Driven cavity

In this section, we investigate a driven cavity flow around a stationary flower-shaped obstacle [24]. No-slip conditions, $\mathbf{u} = (0, 0)$, are applied on the surface of the cavity and on all boundaries of the computational domain $(-1, 1)^2$, except for the upper boundary, which represents a lid moving horizontally at a constant speed, $\mathbf{u} = (1, 0)$. External forces, including gravity, are ignored ($\mathbf{f} = 0$). Fig. 11 depicts the velocity field at time $t = 10s$ using $N_x = 100$ for four Reynolds numbers: $Re = 1, 10, 100, 1000$.

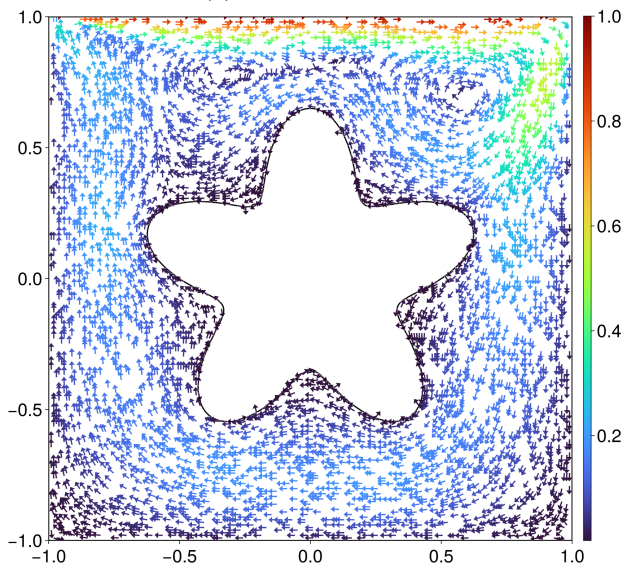
The presence of the flower-shaped object inhibits the development of anticlockwise vortices in the lower corners, which are typically observed in the classical driven cavity configuration without obstacles. Furthermore, the large central clockwise vortex commonly found in the standard case is divided into two distinct vortical structures at low Reynolds numbers ($Re = 1$ and $Re = 10$). This behavior is primarily induced by the reentrant geometry of the flower-shaped object. The centers of these vortices are located approximately at $x = -0.5$ and $x = 0.5$. As the Reynolds number increases to $Re = 100$, the upper-left vortex becomes more asymmetric and shifts slightly to the right. At $Re = 1000$, this vortex disappears, while a new vortex begins to form in the central-right region of the cavity. The resulting flow structures are in good agreement with those reported in [24].



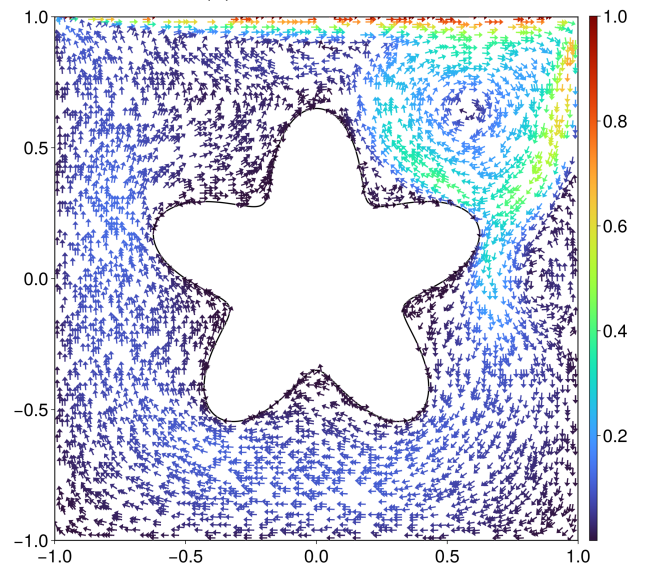
(a) $Re = 1, t = 10s$



(b) $Re = 10, t = 10s$



(c) $Re = 100, t = 10s$



(d) $Re = 1000, t = 10s$

Figure 11: Velocity field for the driven cavity test with $N_x = 100$.

4.5 Flow around a rotating flower-shaped object

In this test, a flower-shaped object rotates anticlockwise about the origin with a constant angular velocity of $\omega = 2\pi/5$ [24]. The fluid is initially at rest, and no-slip boundary conditions are applied on the walls of the computational domain ($\mathbf{u} = 0$) as well as on the boundary of the object ($\mathbf{u}(x, y) = (0, 0, \omega) \times (x, y, 0)$) throughout the simulation. Fig. 12 and Fig. 13 illustrate the velocity field at nine different time steps for a grid resolution of $N_x = 60$, at $Re = 100$ and $Re = 1$, respectively. The moving domain is defined by the time-dependent level set function $\phi(x, y, t) = \phi_0(\tilde{x}(t), \tilde{y}(t))$, where $\phi_0(x, y)$ represents the flower at time $t = 0$, defined in (25), and $(\tilde{x}(t), \tilde{y}(t))$ are given by (29).

When $Re = 1$, vortices are formed in the wake of the petals farther from the tips at all time instants. This behavior arises because, at low Reynolds numbers, diffusion dominates the flow. In contrast, when $Re = 100$, vortices are observed at the tips of the petals of the flower-shaped object at all selected time instants. At this Reynolds number, the flow is no longer diffusion-dominated; consequently, vortices remain closer to the petal tips.

Compared with the results reported in [24] for $Re = 100$, no corner vortices are observed in the present simulations. Moreover, the flow exhibits periodic behavior and does not attain a steady state.

4.6 Flow past oscillating bubbles

Motivated by the main application of this work, namely the study of the sorption kinetics of a surfactant around an oscillating bubble, we consider the flow generated by a bubble undergoing small-amplitude oscillations, resulting in a low Reynolds number flow. In the following test, taken from [5], we observe the fluid-flow past a transversely oscillating bubble, as well as a bubble undergoing ellipsoidal deformation at $Re = 0.1$. The motion of the bubble is described using the parametric equations as:

$$\xi(\theta, t) = \xi_c(t) + \delta_\xi(t) \cos(\theta), \quad \zeta(\theta, t) = \zeta_c(t) + \delta_\zeta(t) \sin(\theta),$$

where $(\xi_c(t), \zeta_c(t))$ denotes the center of the bubble, and $\delta_\xi(t), \delta_\zeta(t)$ control its deformation. The velocity $\mathbf{u}_B(\xi, \zeta) = (u_B(\xi, \zeta), v_B(\xi, \zeta))$ on the surface of the bubble ($\sqrt{\xi^2 + \zeta^2} = R_B$) is given by:

$$u_B(\xi, \zeta) = \xi'_c(t) + \delta'_\xi(t) \cos(\theta), \quad v_B(\xi, \zeta) = \zeta'_c(t) + \delta'_\zeta(t) \sin(\theta), \quad \text{where } \theta = \arctan \zeta/\xi.$$

In the first test, we consider a vertical oscillation of the bubble:

$$\xi(t) = 0, \quad \zeta(t) = A \sin(2\pi\nu t), \quad \delta_\xi(t) = \delta_\zeta(t) = R_B.$$

Next, we model the ellipsoidal deformation as:

$$\xi(t) = \zeta(t) = 0, \quad \delta_\zeta(t) = R_B(1 + A \sin(2\pi\nu t)), \quad \delta_\xi(t) = \sqrt{\frac{R_B^3}{\delta_\zeta(t)}}.$$

We choose $A = 0.01$, $\nu = 10$, and the bubble radius $R_B = 0.258$. No-slip boundary conditions are enforced on the walls ($\mathbf{u} = 0$). The fluid velocity fields at selected fractions of the first oscillation period are shown in Fig. 14 and Fig. 15 for the vertical oscillation and ellipsoidal deformation cases, respectively. In these figures, the pink dashed line represents a fictitious depiction of the bubble, where the oscillation amplitude A has been amplified by a factor of 20 for graphical clarity.

For the transversely oscillating bubble, at $\nu \cdot t = 0.25$, a vortex is observed at $x \simeq 0.5$. By $\nu \cdot t = 0.5$, as the bubble returns to its initial configuration, a vortex forms slightly to the left of $x = 0.5$. At $\nu \cdot t = 0.75$, the vortex moves rightward, and at $\nu \cdot t = 1$, when the bubble again returns to its initial configuration, a new vortex forms slightly to the left of $x = 0.5$. This sequence repeats, demonstrating the periodic behavior of vortex formation induced by the vertical oscillations of the bubble.

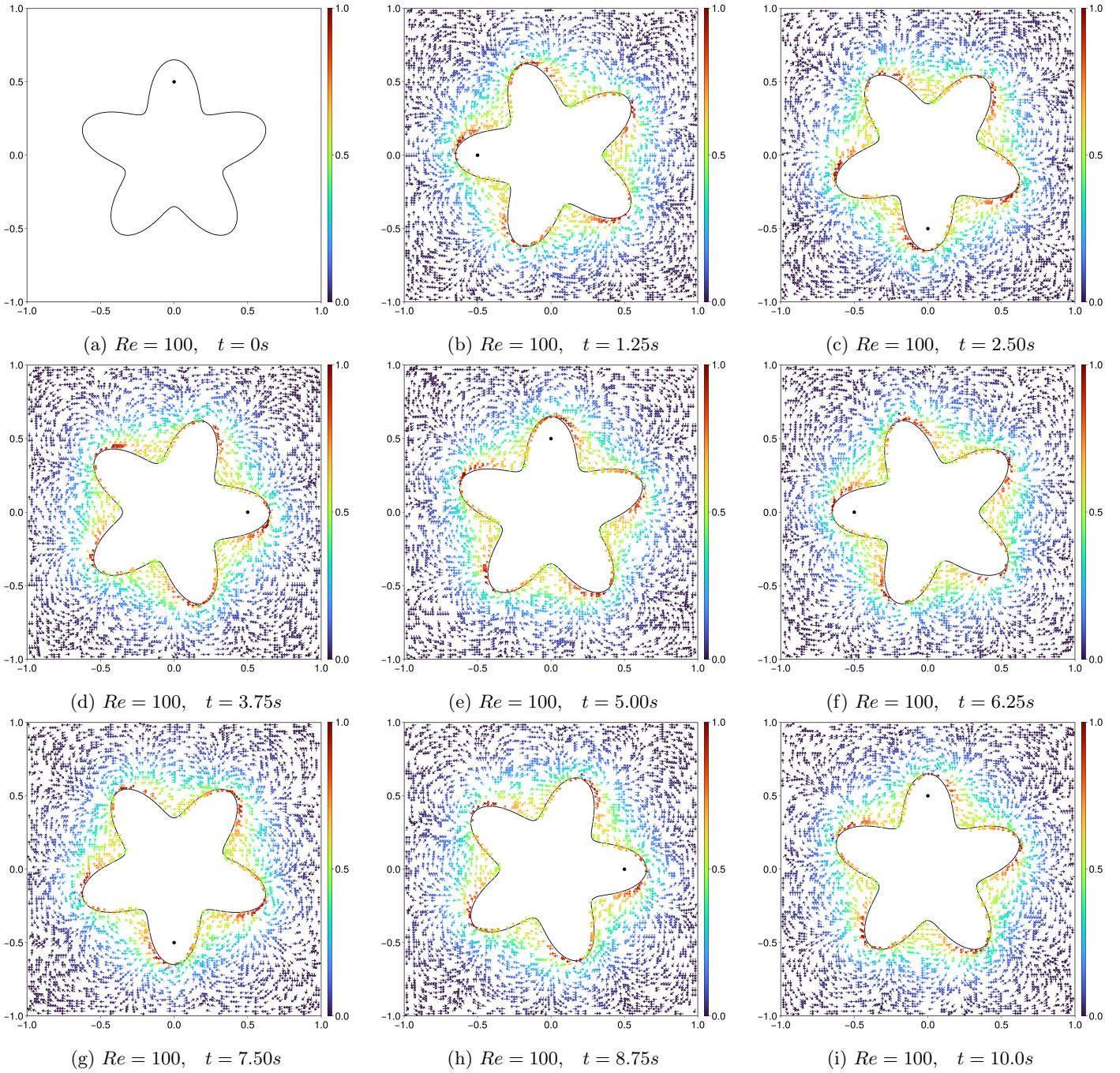


Figure 12: Velocity field at different time instants for the rotating flower-shaped object test with $N_x = 60$ at $Re = 100$. Vortices are formed at the tips of the petals at all selected time instants.

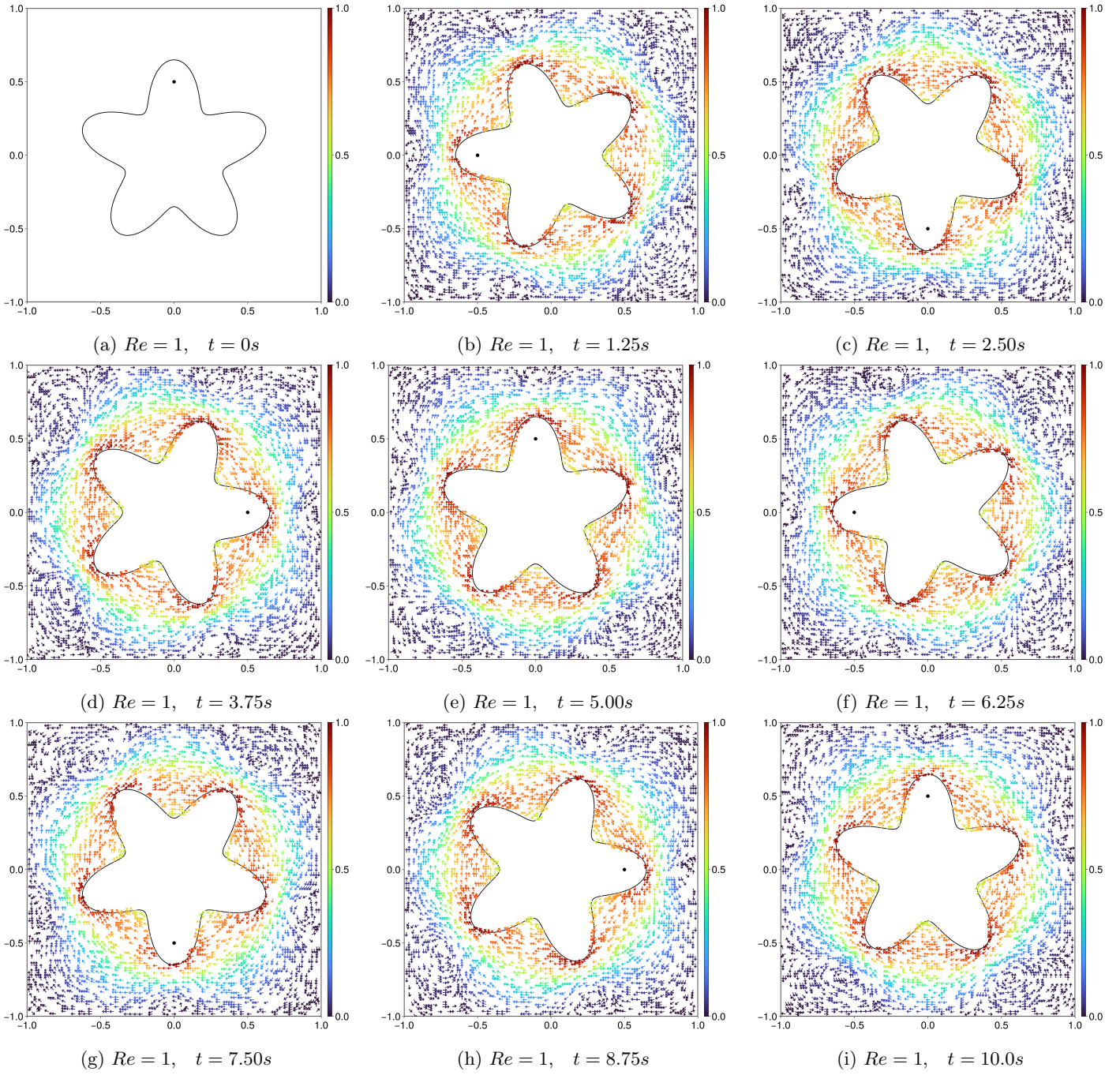


Figure 13: Velocity field at different time instants for the rotating flower-shaped object test with $N_x = 60$ at $Re = 1$. Vortices are observed in the wake of the petals farther from the tips at all time instants.

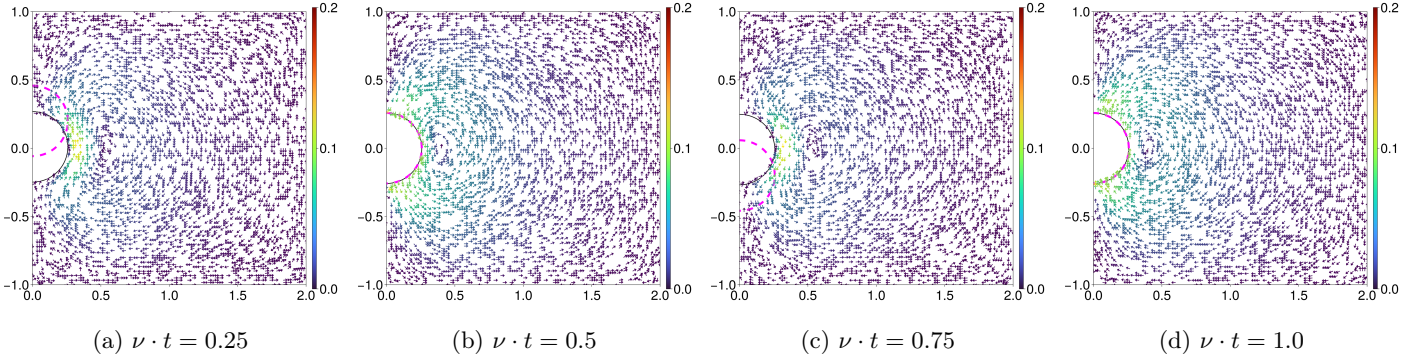


Figure 14: Velocity field for the flow past a transversely oscillating bubble at $Re = 0.1$ at selected fractions of the first oscillation period. The pink dashed line represents a fictitious depiction of the bubble, where the oscillation amplitude A has been amplified by a factor of 20 for graphical clarity.

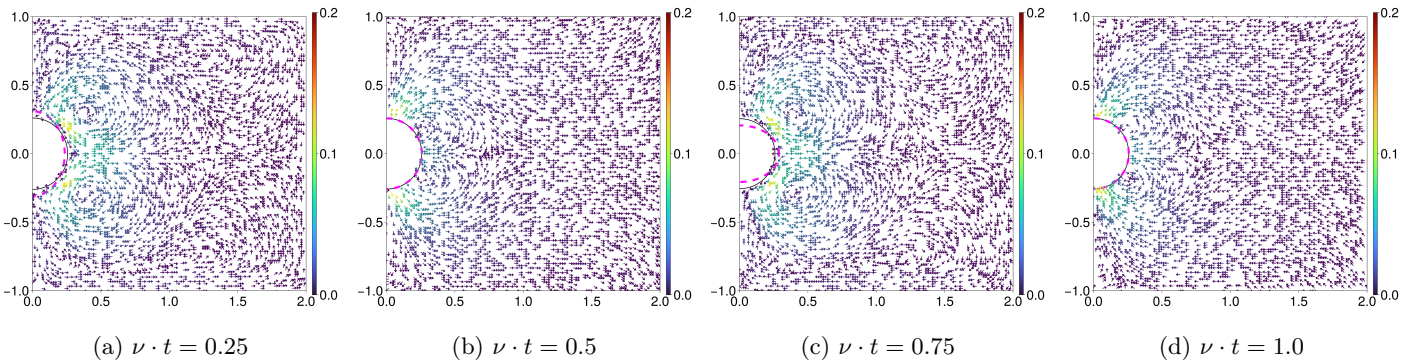


Figure 15: Velocity field for the flow past a bubble undergoing ellipsoidal deformation at $Re = 0.1$ at selected fractions of the first oscillation period. The pink dashed line represents a fictitious depiction of the bubble, where the oscillation amplitude A has been amplified by a factor of 20 for graphical clarity.

For the ellipsoidal deformation of the bubble, at $\nu \cdot t = 0.25$ and at $\nu \cdot t = 0.75$, two vortices are observed to the left of $x \simeq 0.5$, and two vortices appear between $x = 1$ and $x = 1.5$. At $\nu \cdot t = 0.5, 1$, the bubble returns to its initial configuration and two new vortices form near the bubble, while the vortices in the region between $x = 1$ and $x = 1.5$ vanish. This behavior demonstrates the periodic formation of vortices in the wake of the ellipsoidally deforming bubble, as observed in experimental results [54].

5 Conclusions

In this work we introduced a new numerical strategy for approximating the Navier–Stokes equations in arbitrary moving domains. The method combines a ghost finite element discretization in space with high-order IMEX time integrators. By tailoring Aslam’s extrapolation technique to the finite element framework, we successfully extended the scheme to handle domain motion in a robust and geometrically flexible manner. We constructed and analyzed IMEX schemes of different orders, showing that the proposed two-stage and four-stage formulations achieve second- and third-order accuracy in time, respectively. The approximation of the curved boundary by a polygon introduces a second-order geometrical error; higher order spatial discretizations are obtained via the shifted boundary method. The numerical experiments confirm the expected convergence rates both in fixed and moving domains. In particular, the results demonstrate the effectiveness of Aslam extrapolation in preserving accuracy when the computational domain evolves in time.

The aim of this research is the application described in the Introduction section, where an oscillating trap adsorbs the diffusing surfactant. At the current stage, we are able to capture only a one-way coupling, where the surrounding fluid is influenced by the motion of the obstacle. The next step is to incorporate the full two-way interaction, allowing the motion of the vibrating bubble to be affected by the fluid dynamics. This will enable us to simulate a scenario in which a domain contains two bubbles: initially, only one bubble oscillates, generating a fluid motion that subsequently induces oscillations in the second bubble through the surrounding flow.

References

- [1] Arthur W Adamson, Alice Petry Gast, et al. Physical chemistry of surfaces, volume 150. Interscience publishers New York, 1967.
- [2] Tariq D Aslam. A partial differential equation approach to multidimensional extrapolation. Journal of Computational Physics, 193(1):349–355, 2004.
- [3] Clarissa Astuto. Standard versus asymptotic preserving time discretizations for the poisson-nernst-planck system in the quasi-neutral limit. arXiv preprint arXiv:2511.07964, 2025.
- [4] Clarissa Astuto, Daniele Boffi, Giovanni Russo, and Umberto Zerbinati. A nodal ghost method based on variational formulation and regular square grid for elliptic problems on arbitrary domains in two space dimensions. Computer Methods in Applied Mechanics and Engineering, 443:118041, 2025.
- [5] Clarissa Astuto, Armando Coco, and Giovanni Russo. A finite-difference ghost-point multigrid method for multi-scale modelling of sorption kinetics of a surfactant past an oscillating bubble. Journal of Computational Physics, 476:111880, 2023.
- [6] Clarissa Astuto, Armando Coco, and Umberto Zerbinati. A Comparison of the Coco-Russo Scheme and ghost-FEM for elliptic Equations in Arbitrary Domains. Advances in Nonlinear Hyperbolic Partial Differential Equations: Numerical Analysis and Applications, pages 1–21, 2026.

- [7] Clarissa Astuto, Jan Haskovec, Peter Markowich, and Simone Portaro. Self-regulated biological transportation structures with general entropy dissipations, part I: The 1D case. Journal of Dynamics and Games, 2023.
- [8] Clarissa Astuto, Peter Markowich, Simone Portaro, and Giovanni Russo. Self-regulated biological transportation structures with general entropy dissipation: 2D case and leaf-shaped domain. arXiv preprint arXiv:2408.15680, 2024.
- [9] Clarissa Astuto, Antonio Raudino, and Giovanni Russo. Multiscale modeling of sorption kinetics. Multiscale Modeling & Simulation, 21(1):374–399, 2023.
- [10] Clarissa Astuto and Giovanni Russo. Asymptotic preserving and accurate scheme for multiscale poisson-nernst-planck (MPNP) system. arXiv preprint arXiv:2507.01402, 2025.
- [11] Nabil M. Atallah, Claudio Canuto, and Guglielmo Scovazzi. The high-order shifted boundary method and its analysis. Computer Methods in Applied Mechanics and Engineering, 394:114885, May 2022.
- [12] Santiago Badia, Hridya Dilip, and Francesc Verdugo. Space-time unfitted finite element methods for time-dependent problems on moving domains. Computers & Mathematics with Applications, 135:60–76, 2023.
- [13] Santiago Badia and Francesc Verdugo. Gridap: An extensible finite element toolbox in julia. Journal of Open Source Software, 5(52):2520, 2020.
- [14] Santiago Badia, Francesc Verdugo, and Alberto F. Martín. The aggregated unfitted finite element method for elliptic problems. Computer Methods in Applied Mechanics and Engineering, 336:533–553, 2018.
- [15] Daniele Boffi, Franco Brezzi, Michel Fortin, et al. Mixed finite element methods and applications, volume 44. Springer.
- [16] Sebastiano Boscarino, Lorenzo Pareschi, and Giovanni Russo. Implicit-explicit methods for evolutionary partial differential equations. SIAM, 2024.
- [17] Walter Boscheri, Giacomo Dimarco, Raphaël Loubère, Maurizio Tavelli, and Marie-Hélène Vignal. A second order all mach number imex finite volume solver for the three dimensional euler equations. Journal of Computational Physics, 415:109486, 2020.
- [18] Walter Boscheri, Giacomo Dimarco, and Maurizio Tavelli. An efficient second order all mach finite volume solver for the compressible navier–stokes equations. Computer Methods in Applied Mechanics and Engineering, 374:113602, 2021.
- [19] Franco Brezzi and Michel Fortin. Mixed and hybrid finite element methods, volume 15. Springer Science & Business Media, 2012.
- [20] David L. Brown, Ricardo Cortez, and Michael L. Minion. Accurate projection methods for the incompressible navier–stokes equations. Journal of Computational Physics, 168(2):464–499, 2001.
- [21] Lynn Brown, Ganesan Narsimhan, and PC Wankat. Foam fractionation of globular proteins. Biotechnology and Bioengineering, 36(9):947–959, 1990.
- [22] Erik Burman, Susanne Claus, Peter Hansbo, Mats G Larson, and André Massing. Cutfem: discretizing geometry and partial differential equations. International Journal for Numerical Methods in Engineering, 104(7):472–501, 2015.
- [23] Alexandre Joel Chorin. A numerical method for solving incompressible viscous flow problems. Journal of Computational Physics, 135(2):118–125, 1997.

- [24] Armando Coco. A multigrid ghost-point level-set method for incompressible navier-stokes equations on moving domains with curved boundaries. Journal of Computational Physics, 418:109623, 2020.
- [25] Armando Coco and Giovanni Russo. High-order finite-difference ghost-point methods for elliptic problems in domains with curved boundaries. Open Mathematics, 22(1), January 2024.
- [26] R. Courant. Variational methods for the solution of problems of equilibrium and vibrations. Bull. Amer. Math. Soc., 49:1–23, 1943.
- [27] R. Courant and D. Hilbert. Methods of mathematical physics. Vol. I. Interscience Publishers, Inc., New York, N.Y., 1953.
- [28] Victor DeCaria and Michael Schneier. An embedded variable step imex scheme for the incompressible navier–stokes equations. Computer Methods in Applied Mechanics and Engineering, 376:113661, 2021.
- [29] Hridya Dilip and Armando Coco. Multigrid methods for the ghost finite element approximation of elliptic problems. arXiv preprint arXiv:2505.05105, 2025.
- [30] John Dolbow and Isaac Harari. An efficient finite element method for embedded interface problems. International journal for numerical methods in engineering, 78(2):229–252, 2009.
- [31] Alexandre Ern, Jean-Luc Guermond, et al. Finite elements II. Springer, 2021.
- [32] Michel Fortin. Old and new finite elements for incompressible flows. International Journal for numerical methods in fluids, 1(4):347–364, 1981.
- [33] Sashikumaar Ganesan and Lutz Tobiska. Arbitrary lagrangian–eulerian finite-element method for computation of two-phase flows with soluble surfactants. Journal of Computational Physics, 231(9):3685–3702, 2012.
- [34] Wadhah Garhuom, Khuldoon Usman, and Alexander Düster. An eigenvalue stabilization technique to increase the robustness of the finite cell method for finite strain problems. Computational Mechanics, 69(5):1225–1240, 2022.
- [35] Michael Griebel and Marc Alexander Schweitzer. A particle-partition of unity method part v: boundary conditions. In Geometric analysis and nonlinear partial differential equations, pages 519–542. Springer, 2003.
- [36] Peter Hansbo, Mats G Larson, and Sara Zahedi. A cut finite element method for coupled bulk-surface problems on time-dependent domains. Computer Methods in Applied Mechanics and Engineering, 307:96–116, 2016.
- [37] Thomas JR Hughes, Michel Mallet, and Mizukami Akira. A new finite element formulation for computational fluid dynamics: Ii. beyond supg. Computer methods in applied mechanics and engineering, 54(3):341–355, 1986.
- [38] Shi Jin. Efficient asymptotic-preserving (ap) schemes for some multiscale kinetic equations. SIAM Journal on Scientific Computing, 21(2):441–454, 1999.
- [39] Moritz Knoche, Hiroto Tamura, and Martin J Bukovac. Performance and stability of the organosilicon surfactant l-77: effect of ph, concentration, and temperature. Journal of agricultural and food chemistry, 39(1):202–206, 1991.
- [40] Hans Petter Langtangen, Kent-Andre Mardal, and Ragnar Winther. Numerical methods for incompressible viscous flow. Advances in Water Resources, 25(8):1125–1146, 2002.
- [41] Jaesung Lee and C. Pozrikidis. Effect of surfactants on the deformation of drops and bubbles in navier–stokes flow. Computers & Fluids, 35(1):43–60, 2006.

- [42] Randall J LeVeque. Finite volume methods for hyperbolic problems, volume 31. Cambridge university press, 2002.
- [43] Stanley Osher and Ronald Fedkiw. Level set methods and dynamic implicit surfaces, volume 153 of Applied Mathematical Sciences. Springer-Verlag, New York, 2003.
- [44] Stanley. Osher and Ronald P. Fedkiw. Level set methods and dynamic implicit surfaces. Applied mathematical sciences ; 153. Springer, New York ;, 2002.
- [45] Alfio Quarteroni, Fausto Saleri, and Alessandro Veneziani. Factorization methods for the numerical approximation of Navier–Stokes equations. Computer methods in applied mechanics and engineering, 188(1-3):505–526, 2000.
- [46] A. Raudino, D. Raciti, A. Grassi, M. Pannuzzo, and M. Corti. Oscillations of bubble shape cause anomalous surfactant diffusion: Experiments, theory, and simulations. Langmuir, 2016.
- [47] Antonio Raudino, Antonio Grassi, Giuseppe Lombardo, Giovanni Russo, Clarissa Astuto, and Mario Corti. Anomalous sorption kinetics of self-interacting particles by a spherical trap. Communications in Computational Physics, 31(3):707–738, 2022.
- [48] Giovanni Russo and Peter Smereka. A remark on computing distance functions. Journal of computational physics, 163(1):51–67, 2000.
- [49] S. Saberi, G. Meschke, and A. Vogel. The influence of nitsche stabilization on geometric multigrid for the finite cell method, 2023.
- [50] M. Schäfer, S. Turek, F. Durst, E. Krause, and R. Rannacher. Benchmark Computations of Laminar Flow Around a Cylinder, page 547–566. Vieweg+Teubner Verlag, 1996.
- [51] J. A. Sethian. Level set methods and fast marching methods: evolving interfaces in computational geometry, fluid mechanics, computer vision, and materials science. Cambridge monographs on applied and computational mathematics 3. Cambridge University Press, 2nd ed edition, 1999.
- [52] Ting Song, Alex Main, Guglielmo Scovazzi, and Mario Ricchiuto. The shifted boundary method for hyperbolic systems: Embedded domain computations of linear waves and shallow water flows. Journal of Computational Physics, 369:45–79, 2018.
- [53] Mark Sussman, Peter Smereka, and Stanley Osher. A level set approach for computing solutions to incompressible two-phase flow. Journal of computational physics, 114(1):146–159, 1994.
- [54] Paul Tho, Richard Manasseh, and Andrew Ooi. Cavitation microstreaming patterns in single and multiple bubble systems. Journal of fluid mechanics, 576:191–233, 2007.
- [55] Samuel Tomlinson, Frédéric Gibou, Paolo Luzzatto-Fegiz, Fernando Temprano-Coletto, Oliver Jensen, and Julien R Landel. Unsteady evolution of slip and drag in surfactant-contaminated superhydrophobic channels. Journal of Fluid Mechanics, 2023.
- [56] Samuel D Tomlinson, Frédéric Gibou, Paolo Luzzatto-Fegiz, Fernando Temprano-Coletto, Oliver E Jensen, and Julien R Landel. Laminar drag reduction in surfactant-contaminated superhydrophobic channels. Journal of Fluid Mechanics, 963:A10, 2023.
- [57] Jose E Valentini, William R Thomas, Paul Sevenhuysen, Tsung S Jiang, Hae O Lee, Yi Liu, and Shi Chern Yen. Role of dynamic surface tension in slide coating. Industrial & engineering chemistry research, 30(3):453–461, 1991.

- [58] JJIM Van Kan. A second-order accurate pressure-correction scheme for viscous incompressible flow. SIAM journal on scientific and statistical computing, 7(3):870–891, 1986.
- [59] Sachin Velankar, Peter Van Puyvelde, Jan Mewis, and Paula Moldenaers. Effect of compatibilization on the breakup of polymeric drops in shear flow. Journal of Rheology, 45(4):1007–1019, 2001.
- [60] Francesc Verdugo and Santiago Badia. The software design of gridap: A finite element package based on the julia JIT compiler. Computer Physics Communications, 276:108341, July 2022.
- [61] Francesc Verdugo, Eric Neiva, and Santiago Badia. GridapEmbedded. Version 0.9.5, October 2024. Available at <https://github.com/gridap/GridapEmbedded.jl>.
- [62] J Vidal. Thermodynamics. applications in chemical engineering and the petroleum industry; thermodynamique. application au genie chimique et a l’industrie petroliere. 2003.
- [63] H. A. R. Williams and O. E. Jensen. Two-dimensional nonlinear advection–diffusion in a model of surfactant spreading on a thin liquid film. IMA Journal of Applied Mathematics, 66(1):55–82, 01 2001.
- [64] Jian-Jun Xu, Yin Yang, and John Lowengrub. A level-set continuum method for two-phase flows with insoluble surfactant. Journal of Computational Physics, 231(17):5897–5909, 2012.